JGP Journal of General Physiology

RESEARCH ARTICLE

# Kinetic properties of persistent $Na^+$ current orchestrate oscillatory bursting in respiratory neurons

Tadashi Yamanishi[1,2], Hidehiko Koizumi[1], Marco A. Navarro[3], Lorin S. Milescu[3], and Jeffrey C. Smith[1]

**The rhythmic pattern of breathing depends on the pre-Bötzinger complex (preBötC) in the brainstem, a vital circuit that contains a population of neurons with intrinsic oscillatory bursting behavior. Here, we investigate the specific kinetic properties that enable voltage-gated sodium channels to establish oscillatory bursting in preBötC inspiratory neurons, which exhibit an unusually large persistent $Na^+$ current ($I_{NaP}$). We first characterize the kinetics of $I_{NaP}$ in neonatal rat brainstem slices in vitro, using whole-cell patch-clamp and computational modeling, and then test the contribution of $I_{NaP}$ to rhythmic bursting in live neurons, using the dynamic clamp technique. We provide evidence that subthreshold activation, persistence at suprathreshold potentials, slow inactivation, and slow recovery from inactivation are kinetic features of $I_{NaP}$ that regulate all aspects of intrinsic rhythmic bursting in preBötC neurons. The slow and cumulative inactivation of $I_{NaP}$ during the burst active phase controls burst duration and termination, while the slow recovery from inactivation controls the duration of the interburst interval. To demonstrate this mechanism, we develop a Markov state model of $I_{NaP}$ that explains a comprehensive set of voltage clamp data. By adding or subtracting a computer-generated $I_{NaP}$ from a live neuron via dynamic clamp, we are able to convert nonbursters into intrinsic bursters, and vice versa. As a control, we test a model with inactivation features removed. Adding noninactivating $I_{NaP}$ into nonbursters results in a pattern of random transitions between sustained firing and quiescence. The relative amplitude of $I_{NaP}$ is the key factor that separates intrinsic bursters from nonbursters and can change the fraction of intrinsic bursters in the preBötC. $I_{NaP}$ could thus be an important target for regulating network rhythmogenic properties.**

## Introduction

Membrane currents operating at voltages below the spiking threshold may be very small, but they can exert a substantial influence on neuronal activity (Vervaeke et al., 2006; Jackson and Bean, 2007; Milescu et al., 2010b). The persistent $Na^+$ current ($I_{NaP}$) is a tetrodotoxin (TTX)-sensitive subthreshold current found in a wide variety of mammalian central neurons (Crill, 1996; Magistretti et al., 2006; Carter et al., 2012; Yamada-Hanff and Bean, 2013). Relative to the transient current ($I_{NaT}$) generated by all voltage-gated sodium (Nav) channels, $I_{NaP}$ activates at more negative potentials and remains active even under strong depolarization (Maurice et al., 2001; Wu et al., 2005), although in some neurons it exhibits slow inactivation (Fleidervish et al., 1996; Do and Bean, 2003). These properties link $I_{NaP}$ to a diversity of neuronal behaviors, including spontaneous and regular spiking, subthreshold membrane potential oscillations, and oscillatory burst firing (Taddese and Bean, 2002; Sanhueza and Bacigalupo, 2005; Wu et al., 2005; Rotstein et al., 2006; Ziskind-Conhaim et al., 2008).

The molecular identity of $I_{NaP}$ is still unresolved. To our knowledge, $I_{NaP}$ has not been observed without the accompanying large transient component, suggesting that it is not carried by a distinct ion channel. Instead, $I_{NaP}$ is likely to be a kinetic manifestation of the molecular interactions between the Nav pore-forming α subunit and the auxiliary β subunits (Raman et al., 1997; Magistretti and Alonso, 1999; Maurice et al., 2001; Qu et al., 2001; Aman et al., 2009; Bant and Raman, 2010; Chatelier et al., 2010; Chahine and O'Leary, 2011; Lopez-Santiago et al., 2011). The persistence of $I_{NaP}$ under depolarization distinguishes it from the "window" current, which is defined as the steady-state component of $I_{NaT}$, resulting from the overlap of the voltage-de-

[1]Cellular and Systems Neurobiology Section, National Institute of Neurological Disorders and Stroke, National Institutes of Health, Bethesda, MD; [2]The First Department of Oral and Maxillofacial Surgery, Osaka University Graduate School of Dentistry, Osaka, Japan; [3]Division of Biological Sciences, University of Missouri, Columbia, MO.

Correspondence to Lorin S. Milescu: milescul@missouri.edu; Jeffrey C. Smith: smithj2@ninds.nih.gov.

pendent activation and inactivation curves (Attwell et al., 1979; French et al., 1990; Magistretti and Alonso, 1999). Unlike the persistent current, the window current is assumed to vanish quickly and completely under sufficient depolarization.

A circuit that relies on $I_{NaP}$ is the brainstem pre-Bötzinger complex (preBötC), a critical excitatory circuit for respiratory rhythm generation in mammals (Smith et al., 1991; Feldman and Del Negro, 2006; Richter and Smith, 2014). The preBötC contains neurons that express a characteristically large amount of $I_{NaP}$ and exhibit intrinsic rhythmic bursting behavior (Del Negro et al., 2005; Koizumi and Smith, 2008). This intrinsic bursting is proposed to be essential for generating preBötC rhythmic inspiratory activity in certain conditions, such as the fetal (Pagliardini et al., 2003; Chevalier et al., 2016) and neonatal (Smith et al., 1991; Koshiya and Smith, 1999; Peña et al., 2004; Ramirez et al., 2004) preBötC, isolated in vitro and during hypoxia in the adult in vivo (Paton et al., 2006).

Despite existing evidence that strongly connects $I_{NaP}$ to cellular bursting behavior, in respiratory and other central nervous system neurons (Darbon et al., 2004; Wu et al., 2005; Yue et al., 2005; Tazerart et al., 2007; Zhong et al., 2007; Ziskind-Conhaim et al., 2008), we still lack a mechanistic understanding of how $I_{NaP}$ contributes to rhythmic bursting. The limited information on properties of $I_{NaP}$ in preBötC neurons has been obtained from rodent neonatal neurons in brainstem slices in vitro, where patch-clamp recordings of this current have been practical (Del Negro et al., 2002; Koizumi and Smith, 2008). Previous studies have established a connection between $I_{NaP}$ and cellular bursting in preBötC neurons by combining pharmacological and electrophysiological approaches, demonstrating that pharmacological agents that reduce $I_{NaP}$, such as riluzole or low-concentration TTX, abolish rhythmic bursting at cellular, as well as circuit, levels (Del Negro et al., 2002; Koizumi and Smith, 2008). However, these chemicals are not $I_{NaP}$ specific and may alter the availability of the spike-generating $I_{NaT}$ (Song et al., 1997; Urbani and Belluzzi, 2000; Taddese and Bean, 2002), which is obviously necessary for sustained neuronal firing during a burst. More importantly, pharmacological or genetic approaches cannot dissect out the functional $I_{NaP}$ dynamics during the active and silent phases of cellular oscillatory bursting, as required to establish its mechanistic contributions. In particular, these approaches cannot establish whether the inactivation and recovery from inactivation of $I_{NaP}$ play any role in bursting.

To overcome these challenges, we used the dynamic clamp (DC) technique (Sharp et al., 1993; Milescu et al., 2008, 2010b) to test the contribution of $I_{NaP}$ to the rhythmic bursting of preBötC neurons in neonatal rat brainstem slice preparations in vitro. The idea is to modify the electrophysiological profile of the cell by adding or subtracting a computationally generated conductance with kinetic properties matching $I_{NaP}$. If a relatively large amount of $I_{NaP}$ is the determining factor for bursting, we would expect that adding $I_{NaP}$ would convert a nonburster into an intrinsic burster. Conversely, subtracting $I_{NaP}$ would convert an intrinsic burster into a nonburster. Most importantly, the kinetics of the $I_{NaP}$ model can be manipulated to explore the quantitative relationships between $I_{NaP}$ kinetics and bursting properties.

To our knowledge, a data-derived kinetic model of $I_{NaP}$ in respiratory and other neurons does not yet exist, although theoretical models have been proposed before (Butera et al., 1999a,b; Vervaeke et al., 2006). Thus, our first objective was to formulate a Markov state model that quantitatively explains all the kinetic properties of the $I_{NaP}$ expressed in preBötC neurons, particularly slow inactivation. We emphasize that this model describes exclusively the $I_{NaP}$ component of the total TTX-sensitive current; it does not predict the $I_{NaT}$. Through a series of voltage clamp (VC) protocols designed to isolate $I_{NaP}$ from all the other currents in the cell, especially $I_{NaT}$, we found that $I_{NaP}$ inactivates and recovers from inactivation very slowly, with time constants in the range of seconds. Then, we used this model in DC experiments to test whether bursting activity relies on the presence of $I_{NaP}$ and whether $I_{NaP}$ inactivation is necessary. To distinguish between the role of $I_{NaP}$ and the potential role of calcium-related currents (Ramirez et al., 2004), all experiments were performed under bath-applied calcium channel blockers. We found that the kinetic properties of $I_{NaP}$ establish all aspects of oscillatory bursting activity. Thus, $I_{NaP}$ initiates and maintains the active phase of bursting because of its subthreshold voltage activation. Importantly, $I_{NaP}$ terminates the burst by its slow and cumulative inactivation. Finally, $I_{NaP}$ controls bursting frequency by its slow recovery from inactivation. Conceptually, these ideas have been proposed before in modeling studies (Butera et al., 1999a,b; Rybak et al., 2003, 2004), but they have not been experimentally determined and tested.

## Materials and methods

### Animal procedures

All animal procedures were approved by the National Institute of Neurological Disorders and Stroke of the National Institutes of Health and the University of Missouri Animal Care and Use Committees.

### Medullary slice preparation

In vitro medullary slice preparations were obtained from neonatal (postnatal day 0 [P0]–P3) Sprague-Dawley male and female rats, as previously described (Koshiya and Smith, 1999; Koizumi and Smith, 2008). Briefly, the medulla was dissected in artificial cerebrospinal fluid (aCSF) containing the following (in mM): 124 NaCl, 25 $NaHCO_3$, 3 KCl, 1.5 $CaCl_2$, 1 $MgSO_4$, 0.5 $NaH_2PO_4$, and 30 D-glucose, equilibrated with 95% $O_2$ and 5% $CO_2$ (pH 7.4 ± 0.05 at room temperature). Transverse slices (300–350-µm thick) containing the preBötC and the rostral end of the hypoglossal (XII) motor nucleus, including XII nerve rootlets (Fig. 1 A), were transferred to the recording chamber and superfused with aCSF warmed to 27°C. Only one slice was obtained per animal. Bursting behavior has been observed in preBötC neurons at 3 mM extracellular $K^+$ concentration ($[K^+]_o$) in situ (St.-John et al., 2009). However, to enable robust rhythmic respiratory activity and minimize animal usage, we elevated $[K^+]_o$ to 8 mM. Although experimental conditions with higher $[K^+]_o$ may alter bursting properties in some types of neurons, such as hippocampal pyramidal cells (Jensen et al., 1994), the rhythmic bursting behavior of preBötC inspiratory neurons was shown to be minimally affected by changes in $[K^+]_o$ (Tryba et al., 2003).

### Neuron identification

All patch-clamp whole-cell recordings were obtained from neurons located at depths ≥100 µm within the slice, under infrared differential interference contrast visualization or through a blind-patch approach. PreBötC neurons were identified based on their location in the slice. Respiratory neurons were confirmed based on their firing activity in phase with the hypoglossal (XII) nerve output (Fig. 1 B). Neurons were classified as intrinsic bursters if they maintained rhythmic bursting activity under bath-applied synaptic transmission blockers. For cells targeted for VC experiments, when channel blockers were added to the intracellular solution, neuronal identity was determined before gigaseal formation, in current clamp (CC) mode.

### Pipette solutions

For VC, the electrodes were filled with a solution containing (in mM): 70 Cs-gluconate, 30 Na-gluconate, 10 TEA-Cl, 5 4-aminopyridine, 10 EGTA, 1 $CaCl_2$, 15 HEPES, 4 Mg-ATP, 0.3 Na-GTP, and 10 $Na_2$-phosphocreatine, pH 7.3, adjusted with CsOH (285 ± 5 mOsm/liter). $Cs^+$, $TEA^+$, and 4-aminopyridine minimized $K^+$ currents, whereas the high $Na^+$ concentration decreased the reversal potential of $Na^+$ currents, reducing VC artifacts. For CC or dynamic clamp (DC), the electrodes were filled with a solution containing (in mM): 125 K-gluconate, 4 NaCl, 11 EGTA, 1 $CaCl_2$, 10 HEPES, 4 Mg-ATP, 0.3 Na-GTP, and 4 $Na_2$-phosphocreatine, pH 7.3 adjusted with KOH (285 ± 5 mOsm/liter).

### Pharmacology

To block sodium currents, TTX (1 µM) was added to the superfusing aCSF. $Ca^{2+}$-related currents, including voltage-sensitive $Ca^{2+}$ currents and $Ca^{2+}$-activated currents, and depolarization-evoked neurotransmitter release were minimized with bath-applied $CdCl_2$ (200 µM). Non-NMDA (N-methyl-D-aspartate) glutamate receptors, which mediate excitatory synaptic connections among preBötC neurons, were blocked with 6-cyano-7-nitroquinoxaline-2,3-dione (CNQX, 20 µM; Koshiya and Smith, 1999). Each bath-applied drug was used only once in a given slice. All reagents were purchased from Sigma-Aldrich.

### Electrophysiology

Recording electrodes (3–4 MΩ) were pulled from borosilicate glass (WPI) and coated with Sylgard to reduce capacitive transients, which is critical for stable operation under DC. Pipette capacitance was compensated 100% in VC and ≈70% in CC and DC. Under VC, the series resistance ($R_s$) was compensated ≈80% (2-µs response time) and readjusted before running a protocol. The neuronal membrane capacitance was approximated as the value necessary to compensate the slow capacitive component. In CC and DC experiments, $R_s$ was compensated 100% and readjusted as necessary. A liquid junction potential of ≈10 mV for the $K^+$-based and ≈8 mV for the $Cs^+$-based solutions was corrected online. Somatic whole-cell recordings were obtained with an EPC-9 or EPC-10 patch-clamp amplifier (HEKA Electronics) controlled by Pulse 8.77 software (HEKA Electronics). VC protocols were constructed and applied with Pulse software. The membrane current was low-pass filtered at 10 kHz and digitally sampled at 50 kHz, using the amplifier's built-in digitizer. For CC or DC recordings, the membrane voltage was sampled at 10 kHz using a PowerLab A/D converter and recorded with Chart software (AD Instruments).

### VC protocols

The total TTX-sensitive $Na^+$ current flowing during a burst was obtained with synthetic burst waveforms that were applied as voltage commands in VC, as shown in Fig. 2 (C and D). One waveform pattern is a construct that statistically matches the experimentally observed bursts in terms of voltage time course, spike count, and frequency ("realistic" burst waveform; Fig. 2 C, upper trace), whereas the other waveform contains a series of identical action potentials separated by a constant 20-ms interspike interval ("uniform" burst waveform; Fig. 2 D, upper trace). To characterize the kinetic properties of $I_{NaP}$, we designed VC protocols that isolate the persistent from the transient component of the TTX-sensitive $Na^+$ current, based on differences in their timing and voltage dependence (Fig. 3 A–F). To better isolate the relatively small $I_{NaP}$ from all other membrane currents and experimental artifacts, all protocols were constructed with P/4 leak subtraction and were repeated under bath-applied TTX (1 µM) for TTX subtraction. Neurons with evidence of poor space-clamp (unclamped action potential currents) were excluded from analysis.

### $I_{NaP}$ modeling

The main $I_{NaP}$ model developed in this study (Model 1; Fig. 4 A) was obtained by fitting multiple VC datasets simultaneously (Fig. 4, B–E), as previously described (Milescu et al., 2010b). A second model (Model 2; Fig. 7 A) was derived by removing all inactivated states from Model 1 and adjusting the remaining rates to match a subset of VC data (Fig. 7, B and C). All rate constants were expressed as exponential functions of voltage: $k_{ij} = k_{ij}^0 \times e^{k_{ij}^1 \times V}$, where $k_{ij}$ is the rate constant of the transition between states $i$ and $j$ (in $ms^{-1}$), $k_{ij}^0$ is a preexponential parameter equal to the rate at zero membrane potential (in $ms^{-1}$), $k_{ij}^1$ is an exponential parameter describing the voltage sensitivity (in $mV^{-1}$), and $V$ is the voltage (in mV). In Model 1, allosteric relationships between rate constants are indicated by the $a$ and $b$ factors (Fig. 4 A). The kinetic parameters $k_{ij}^0$ and $k_{ij}^1$ and the allosteric factors $a$ and $b$ were optimized with QuB software, as previously described (Milescu et al., 2008, 2010b), enforcing microscopic reversibility and all other constraints implied by the model (Navarro et al., 2018; Salari et al., 2018). The predictions of the model, as required during the optimization process for a given set of parameters, were calculated in response to the same voltage protocols as used experimentally to record the data. The differential equations describing the time course of state occupancies were integrated using the matrix method (Milescu et al., 2008; Salari et al., 2016). The cost function was calculated as the average sum of square errors between the data and the prediction of the model. The components of the cost function were weighted so as to balance the goodness of fit between the different datasets. For this, conductance or current datasets (e.g., activation and inactivation time course) were normalized to span a range of −1 to 1 to match those datasets that express a fraction (e.g., availability or recovery) and span a 0-to-1 range.

The optimization was performed with the "simplex" search engine, which was restarted several times with different initial parameter values, to avoid local minima. The optimizer was allowed to run for 300 iterations or until none of the free parameters changed more than 0.0001 between two consecutive iterations. The parameter estimates are given in Table 1. For Model 1, the following parameters were estimated directly: $k_a^0$, $k_a^1$, $k_d^0$, $k_d^1$, $k_o^0$, $k_o^1$, $k_c^0$, $k_c^1$, $k_i^0$, $k_i^1$, $k_r^0$, $k_r^1$, $k_{io}^0$, $k_{ro}^0$, $k_{is}^0$, $k_{is}^1$, $k_{rs}^0$, $k_{rs}^1$, $k_{iso}^0$, $k_{rso}^0$, $a$, and $b$. The remaining parameters were calculated as follows: $k_{io}^1 = k_i^1$, $k_{ro}^1 = k_r^1$, $k_{iso}^1 = k_{is}^1$, $k_{rso}^1 = k_{rs}^1$, $k_{oi}^0 = (k_o^0 + k_c^0)/[1 + ((k_c^0/k_o^0) \times (k_i^0/k_r^0) \times (k_{ro}^0/k_{io}^0) \times a^3 \times b^3)]$, $k_{oi}^1 = k_o^1$, $k_{ci}^0 = (k_o^0 + k_c^0)/[1 + ((k_o^0/k_c^0) \times (k_r^0/k_i^0) \times (k_{io}^0/k_{ro}^0) \times a^{-3} \times b^{-3})]$, $k_{ci}^1 = k_c^1$, $k_{os}^0 = (k_o^0 + k_c^0)/[1 + ((k_c^0/k_o^0) \times (k_{is}^0/k_{rs}^0) \times (k_{rso}^0/k_{iso}^0))]$, $k_{os}^1 = k_o^1$, $k_{cs}^0 = (k_o^0 + k_c^0)/[1 + ((k_o^0/k_c^0) \times (k_{rs}^0/k_{is}^0) \times (k_{iso}^0/k_{rso}^0))]$, and $k_{cs}^1 = k_c^1$. The calculations of $k_{oi}^0$, $k_{ci}^0$, $k_{os}^0$, and $k_{cs}^0$ not only preserve microscopic reversibility, but also ensure the same time constant for the $SI_{11}$–$SI_{12}$ and $I_9$–$I_{10}$ transitions as for $C_4$–$O_5$, further reducing the number of free parameters down to 22. To obtain the standard deviations of the estimates, which are not intrinsically computed by the simplex algorithm, we calculated a numerical approximation of the Hessian of the cost function and inverted it to produce the covariance matrix. The parameter standard deviations (Table 1) were obtained as the square root of the diagonal entries in the covariance matrix.

### Neuronal modeling

As shown in Fig. 5, Model 1 was tested with simulations of a single-compartment preBötC neuronal model, as previously formulated (Butera et al., 1999a,b), but modified by replacing the Hodgkin–Huxley-type $I_{NaP}$ model with our data-derived Markov Model 1. Besides $I_{NaP}$, the model includes a spike-generating $Na^+$ current ($I_{NaT}$), a delayed-rectifier-like $K^+$ current ($I_{DRK}$), and a $K^+$-dominated leak current ($I_{Leak}$). To reflect more recent studies (Koizumi and Smith, 2008; Koizumi et al., 2013) and the present data, several parameters were updated as follows: membrane capacitance ($C_m$ = 27 nS), $I_{NaT}$ half-activation voltage ($V_{1/2}$ = −34.0 mV), $K^+$ Nernst potential ($E_K$ = −72 mV), $I_{NaT}$ conductance ($G_{NaT}$ = 25 nS), and $I_{DRK}$ conductance ($G_{DRK}$ = 15 nS). Numerical simulations were run with QuB software (Milescu et al., 2008), using an integration step of 20 µs.

### CC data analysis

CC recordings were analyzed to quantify cellular bursting properties (burst duration, bursting frequency, action potential count, interspike interval, and burst afterhyperpolarization [bAHP]), as summarized in Fig. 1 E. These values were calculated offline using Chart v5.0 and Igor Pro (Wavemetrics) with custom automated analysis procedures and hand checked for accuracy. A representative set of values was obtained from at least five consecutive bursts sampled from each intrinsic burster that we recorded from, examples of which are shown in Fig. 1 (C and D). Bursting frequency was calculated as the inverse of the time interval measured between two consecutive bursts, using the first action potential in the burst as the reference.

### DC

To test the $I_{NaP}$ Markov models in live neurons (Milescu et al., 2010b; Salari et al., 2016), we used the DC functionality in the QuB software (Milescu et al., 2008) to add or subtract a model-based $I_{NaP}$ to or from nonbursters and bursters. To subtract, we set the conductance ($G_{NaP}$) to a negative value. To solve the $I_{NaP}$ models in real time, we used the matrix method to integrate the differential equations and determine state probabilities (Milescu et al., 2008). Briefly, the state probability vector is updated at every time step using the equation $\mathbf{P}_{t+dt} = \mathbf{P}_t \times e^{\mathbf{Q}_V \times dt}$, where $\mathbf{Q}_V$ is the rate matrix at the measured voltage $V$, $t$ is the real time, and $dt$ is the real time step. The quantity $e^{\mathbf{Q}_V \times dt}$ was precalculated across a range of −80 to +40 mV every 0.5 mV and recalculated each time a kinetic parameter was changed. The refresh rate of the DC system was set to 40 kHz ($dt$ = 25 µs), which allowed the software to simultaneously run the $I_{NaP}$ Markov model, visualize the model output and data in real time, and save to disk multiple channels of data. The DC software was run under Microsoft Windows XP Pro on a dual-processor 2.8-GHz AMD Opteron computer, using a National Instruments 6052E data acquisition card and NI-DAQmx 8.1 driver, interfaced with a HEKA EPC9 or EPC10 patch-clamp amplifier.

## Results

### Intrinsic bursting behavior in preBötC inspiratory neurons

To understand the functional context of $I_{NaP}$, we first examined the firing properties of preBötC inspiratory neurons in medullary slice preparations obtained from neonatal rats (Fig. 1 A). In this preparation, all preBötC inspiratory neurons fire short bursts of action potentials in synchrony with inspiratory network activity, as recorded from the XII motor nerve (Fig. 1 B). However, two electrophysiologically distinct neuronal populations emerge when excitatory, non-NMDA glutamatergic synaptic interactions are blocked by bath application of CNQX (20 µM), which synaptically uncouples inspiratory neurons and disrupts network synchrony (Koshiya and Smith, 1999). Thus, some neurons (intrinsic bursters) continue to exhibit a pattern of oscillatory bursting (Fig. 1 C), whereas other neurons (nonbursters) turn quiet or fire isolated action potentials, but switch to a regimen of sustained firing when sufficiently depolarized via applied current (not depicted), as previously reported (Thoby-Brisson and Ramirez, 2001; Peña et al., 2004; Koizumi et al., 2013). The intrinsic bursters also exhibit voltage dependence. They burst with a frequency that increases monotonically with the level of depolarization (Fig. 1 C) and eventually turn to a regimen of tonic spiking under sufficiently strong depolarization (Koshiya and Smith, 1999; Del Negro et al., 2002; Koizumi et al., 2013), as originally predicted from models (Butera et al., 1999a,b).

### Intrinsic bursters do not rely on $Ca^{2+}$-related currents for bursting

We hypothesize that $I_{NaP}$ plays the key role, but other currents may also give rise to bursting activity. A good candidate is the $Cd^{2+}$-sensitive, $Ca^{2+}$-activated, nonselective cationic current

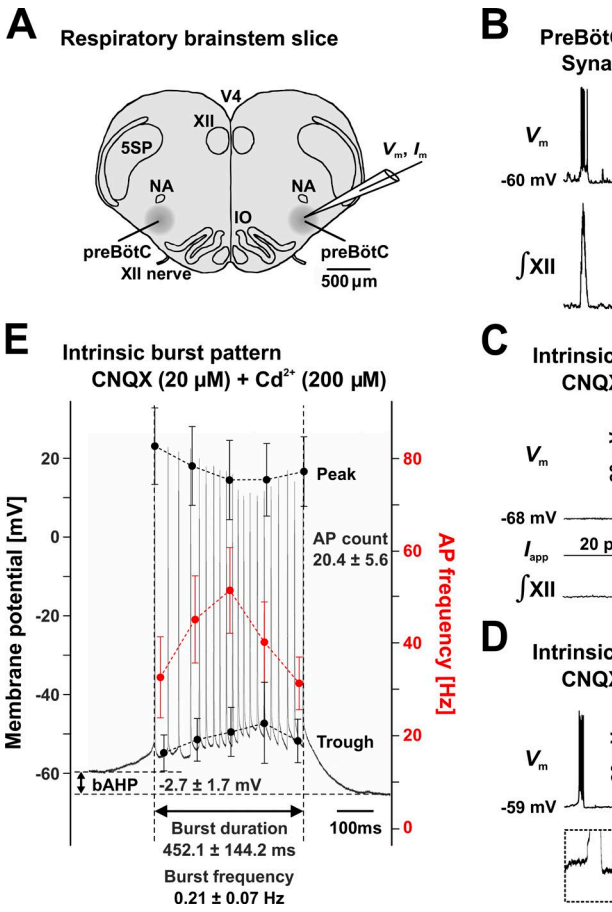


Figure 1. **Intrinsically oscillatory bursting neurons in the preBötC. (A)** Schematic representation of the neonatal rat medullary transverse slice preparation (thickness: 300–350 µm), containing the inspiratory rhythm-generating circuits in the preBötC, with output to the hypoglossal motor nucleus. 5SP, spinal trigeminal nucleus; IO, inferior olivary nucleus; NA, nucleus ambiguus; V4, fourth ventricle; XII, hypoglossal motor nucleus. **(B)** With synaptic transmission intact, inspiratory neurons exhibit rhythmic bursting activity (upper trace, CC recording) in synchrony with inspiratory network activity (lower trace, XII motor nerve inspiratory discharge). **(C)** Intrinsic bursters maintain voltage-dependent rhythmic bursting activity (upper traces) when network-wide synaptic transmission is disrupted by bath-applied CNQX, which blocks non-NMDA glutamatergic receptors. No rhythmic XII nerve output can be observed (lower traces). Neuronal bursting frequency is a function of baseline membrane potential and can be modulated by injecting current ($I_{app}$, middle traces). **(D)** Intrinsic bursting activity is not significantly affected by bath-applied $Cd^{2+}$, which inhibits calcium-related currents. The inset illustrates the characteristic bAHP and the slow depolarization drift (arrow). **(E)** Representative burst (gray trace) and statistical measures. The data points (mean and SD) were calculated at 0%, 25%, 50%, 75%, and 100% of burst time and were obtained from 19 neurons by averaging over five consecutive bursts in each neuron. All CC traces were obtained from representative neurons. AP, action potential.

($I_{CAN}$) that has been identified as the main burst-generating current in several mouse brainstem preparations (Thoby-Brisson and Ramirez, 2001; Peña et al., 2004; Del Negro et al., 2005; Pace et al., 2007; Zavala-Tecuapetla et al., 2008; Rubin et al., 2009). However, recent work from our group has demonstrated that TRPM4-mediated $I_{CAN}$ is mostly involved in regulating burst amplitude, rather than rhythm generation (Koizumi et al., 2018). Nevertheless, to rule out the potential contribution of $I_{CAN}$ to intrinsic bursting in our specific experimental preparation, we first tested whether intrinsic bursting—as identified under synaptic block with CNQX—is maintained under bath application of $Cd^{2+}$ (200 µM), which blocks or inhibits $Ca^{2+}$-related currents and synaptic transmission.

We found that none of the 73 intrinsic bursters identified in this study were $Cd^{2+}$ sensitive, as they all maintained oscillatory bursting under $Cd^{2+}$, with just minor changes in their firing characteristics (Fig. 1 D). $Cd^{2+}$ application typically caused a small baseline membrane hyperpolarization (≤2 mV), but no significant change in burst duration and bursting frequency (not depicted), consistent with our previous observations that bursting can occur in the absence of extracellular $Ca^{2+}$ (Del Negro et al., 2001). Interestingly, each burst ends with a small but significant (≈3 mV) bAHP, followed by a slow depolarization drift toward the next burst (Fig. 1 D), with rare isolated action potentials (not present in this example). A representative burst pattern and statistical features are shown in Fig. 1 E. Although we can conclude that in our in vitro preparation $Ca^{2+}$-related currents do not seem to play a significant role in bursting, we performed all further experiments under bath-applied CNQX and $Cd^{2+}$ to eliminate any potential ambiguity and focus on $I_{NaP}$.

### Supra- and subthreshold burst currents

Even though a single current may be the key factor in establishing a specific pattern of firing activity (e.g., rhythmic bursting), all currents in the cell—sub- and suprathreshold—must interact appropriately to enable that behavior. To understand these interactions, we examined the dynamics of the net current, which can be obtained conveniently from the time derivative of the membrane potential, according to equation $I = -C \times dV/dt$, where $I$ is the total ionic current, $C$ is the estimated membrane capacitance, and $V$ is the membrane potential, as recorded under CC (Fig. 2 A). As a first-order approximation and considering that $Ca^{2+}$-dependent currents were blocked, the inward phase of the net current represents the spike-generating $I_{NaT}$, and the outward phase represents the spike-terminating $K^+$ currents. Within a burst, the inward and outward peak currents progressively decay at first, but then slightly recover and remain steady (Fig. 2 B). The balance between inward and outward transient currents seems to remain steady throughout the burst, suggesting that burst termination is caused neither by a cumulative inactivation of the spike-gen-

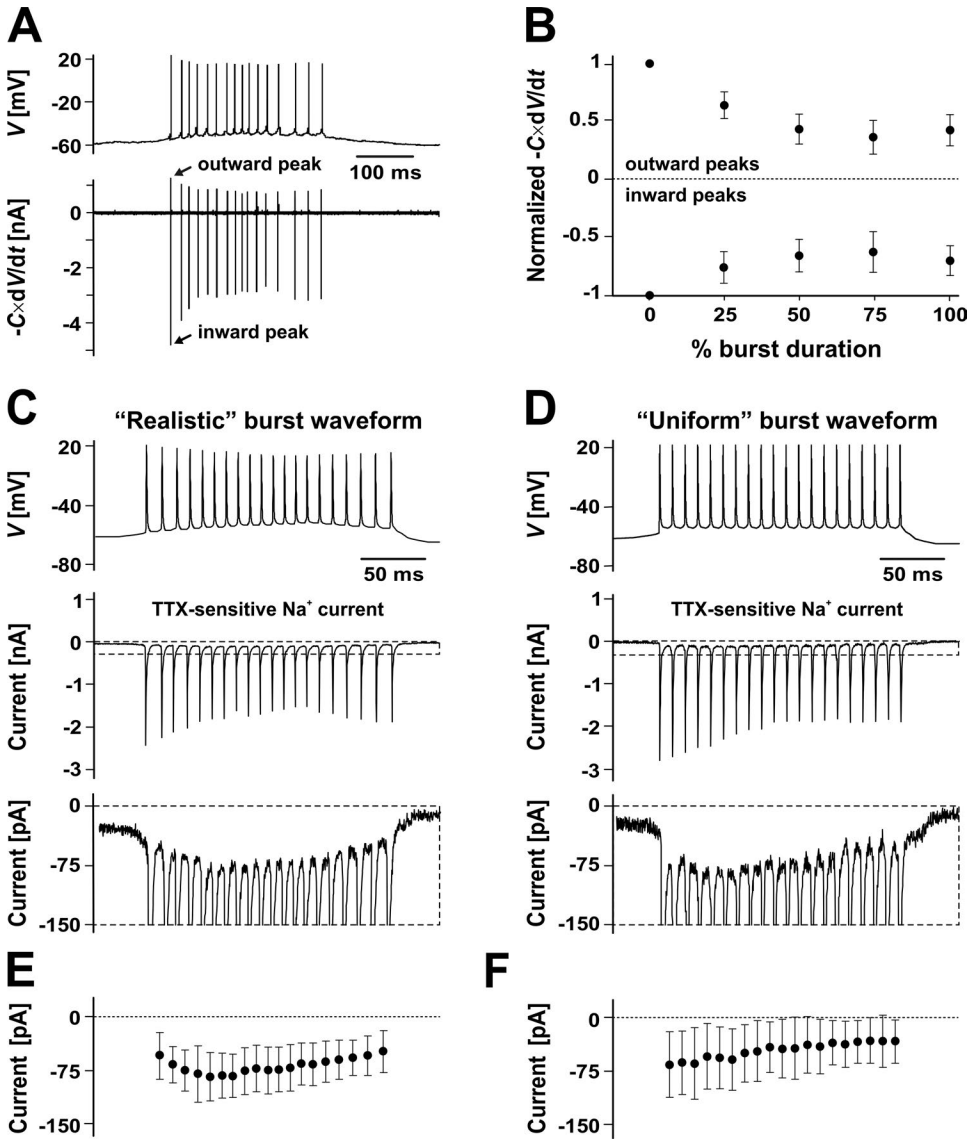


Figure 2. **Supra- and subthreshold burst currents in preBötC intrinsic bursters. (A)** Representative burst waveform (upper trace, CC recording) obtained under bath-applied CNQX (20 μM) and $Cd^{2+}$ (200 μM). The net ionic current (lower trace) was calculated as the negative time derivative of membrane potential, $-C \times dV/dt$, where $C$ is the estimated membrane capacitance. **(B)** Normalized peak inward and outward net current, as measured throughout the burst ($n$ = 19 neurons, each point averaged over five consecutive bursts; mean and SD). **(C and D)** TTX-sensitive $Na^+$ current evoked by synthetic burst waveforms applied as the command voltage in VC. **(C)** Realistic burst waveform (upper trace) statistically matching natural bursts (see Fig. 1 E and Table 2) and evoked current from a representative neuron (middle trace, with dashed line range expanded in the lower trace). **(D)** Same as in C, with a uniform burst waveform, with identical action potentials and constant interspike interval. **(E and F)** The TTX-sensitive $Na^+$ current evoked by the realistic (E) and uniform (F) waveforms, calculated across the 5 ms immediately preceding each action potential ($n$ = 4; mean and SD). Note the exponential decay in F.

erating $I_{NaT}$ nor by a progressive activation of spike-terminating outward currents.

Next, we isolated and examined the TTX-sensitive current. To obtain this current as it would actually flow during a burst, we evoked it with synthetic burst waveforms applied as the voltage command, as detailed in Materials and methods (de Hass and Vogel, 1989). First, we constructed and tested a realistic burst waveform (Fig. 2 C) that statistically resembles the natural bursts (Fig. 1 E). Under this waveform, the transient, suprathreshold $Na^+$ current matches the overall trend of the inward net current (Fig. 2 A). Most importantly, this experiment uncovers a sizable $Na^+$ current that flows before and after the burst, as well as in the interspike interval. Considering the voltage and timing, this current should consist mostly of $I_{NaP}$, with some possible $I_{NaT}$ residual in the interspike interval. Interestingly, the amplitude of the subthreshold $Na^+$ current is smaller after the burst terminates than before it starts and exhibits an overall pattern of decay within the burst (Fig. 2 E).

To more clearly examine the change in the subthreshold $Na^+$ current under the repetitive firing within the burst, we constructed and tested a uniform burst waveform (Fig. 2 D). This synthetic burst contains a train of identical spikes, separated by constant 20-ms intervals, and thus is not representative of the experimentally observed bursts. However, this uniform pattern

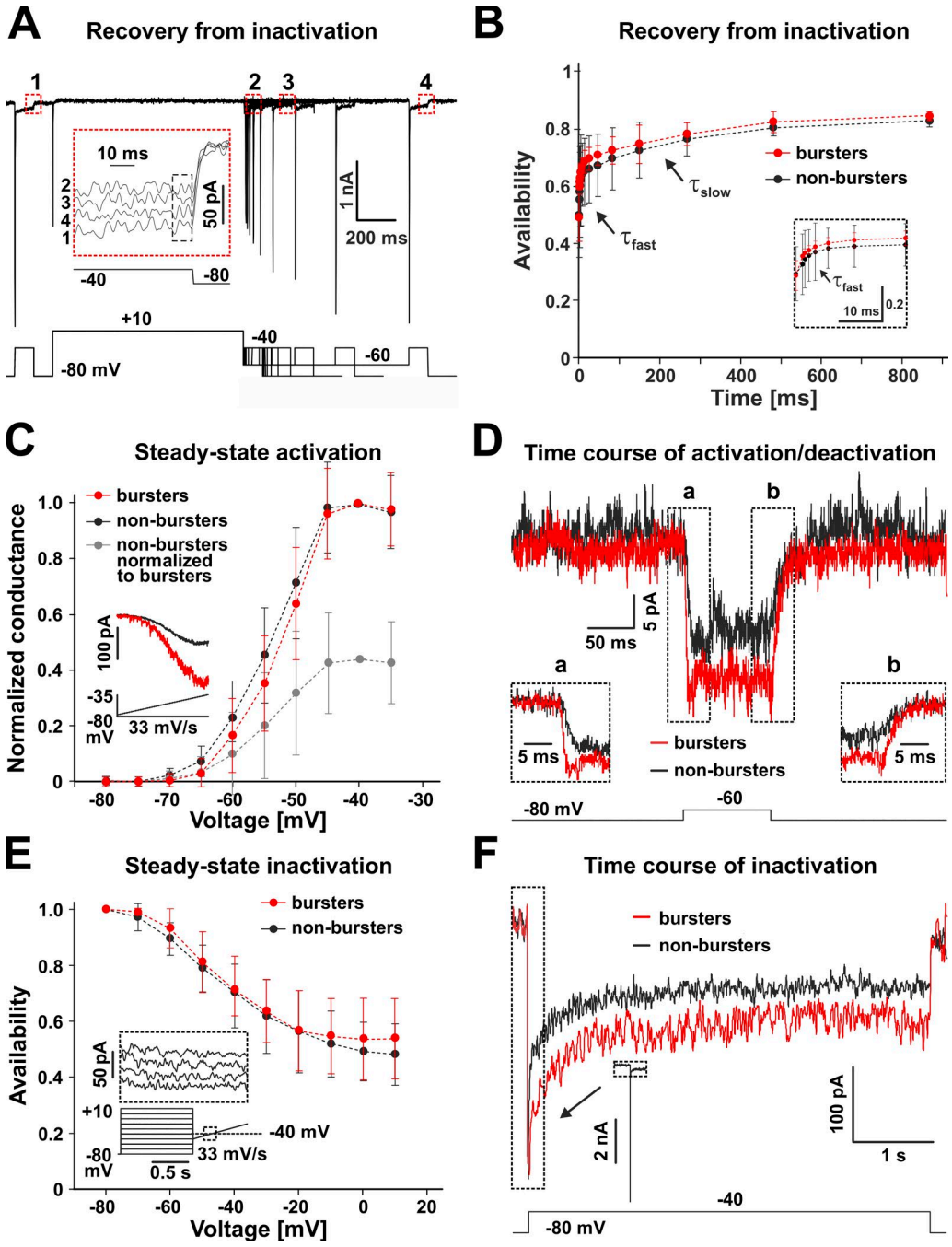


Figure 3. **Kinetic properties of $I_{NaP}$.** TTX-sensitive $Na^+$ currents obtained from preBötC respiratory intrinsic bursters and nonbursters, with TTX subtraction. Representative data shown. **(A)** VC protocol designed to isolate $I_{NaP}$ and test its recovery from inactivation (example data from an intrinsic burster). **(B)** Biexponential recovery from inactivation. The time course is not significantly different (ANOVA, P = 0.51) between intrinsic bursters (red, $n$ = 8) and nonbursters ($n$ = 16). From the combined data, $\tau_{fast}$ = 1.4 ± 0.5 ms and $\tau_{slow}$ = 2.6 ± 0.4 s. **(C)** Steady-state activation curve (inset shows protocol and evoked current). The half-activation voltage ($V_h$) and slope factor ($k$) are not significantly different (unpaired $t$; $V_h$, P = 0.70; $k$, P = 0.39) between bursters ($V_h$ = −47.7 ± 2.5 mV, $k$ = 3.6 ± 0.6 mV; $n$ = 8) and nonbursters ($V_h$ = −48.4 ± 4.0 mV, $k$ = 4.3 ± 1.6 mV; $n$ = 16). The maximum current ($I_{NaP}$*) and conductance ($G_{NaP}$*) values are significantly different (unpaired $t$; P = 0.00043) between bursters ($I_{NaP}$* = 227.7 ± 54.1 pA and $G_{NaP}$* = 2.3 ± 0.5 nS) and nonbursters ($I_{NaP}$* = 106.1 ± 38.7 pA and $G_{NaP}$* = 1.1 ± 0.4 nS). **(D)** Time course of activation (a) and deactivation (b). The time constants of activation ($\tau_a$) and deactivation ($\tau_d$) are similar (unpaired $t$; activation, P = 0.33; deactivation, P = 0.81) between bursters ($n$ = 4) and nonbursters ($n$ = 7). From the combined data, $\tau_a$ = 3.4 ± 1.0 ms and $\tau_d$ = 7.9 ± 2.3 ms. **(E)** Steady-state inactivation curve (inset shows protocol and evoked current). The half-inactivation voltage and slope values are similar (unpaired $t$; $V_h$, P = 0.16; $k$, P = 0.17) between bursters ($V_h$ = −39.1 ± 2.9 mV, $k$ = −9.5 ± 1.2 mV; $n$ = 4) and nonbursters ($V_h$ = −41.8 ± 3.9 mV, $k$ = −11.4 ± 3.1 mV; $n$ = 8). **(F)** Time course of slow inactivation. The time constant of slow decay ($\tau_i$) is similar (unpaired $t$; P = 0.33) between bursters ($n$ = 5) and nonbursters ($n$ = 9). From the combined data, $\tau_i$ = 571.0 ± 50.9 ms. Data shown in B, C, and E are mean ± SD.

eliminates the potential confusion brought by a nonstationary driving force, emphasizing instead the kinetic effects of the current. The subthreshold $Na^+$ current evoked by this burst waveform also exhibits an overall reduction in amplitude throughout

Table 1. **Model parameters**

| Parameter | $k^0$ [ms$^{-1}$] | $k^1$ [mV$^{-1}$] |
|---|---|---|
| Model 1 | | |
| $k_a$ | 21.066 ± 3.341 | 0.025607 ± 0.003094 |
| $k_d$ | 4.9846 ± 0.7914 | −0.041864 ± 0.003096 |
| $k_o$ | 79.237 ± 26.85 | 0.012616 ± 0.007132 |
| $k_c$ | 0.19986 ± 0.0667 | −0.0042279 ± 0.006837 |
| $k_{oi}$ | 4,059.03 | 0.012616 |
| $k_{ci}$ | 75,377.9 | −0.0042279 |
| $k_{os}$ | 14,288.7 | 0.012616 |
| $k_{cs}$ | 65,148.3 | −0.0042279 |
| $k_i$ | 0.0041372 ± 0.003587 | 0.0081037 ± 0.02083 |
| $k_r$ | 0.025486 ± 0.006448 | −0.035336 ± 0.005562 |
| $k_{io}$ | 0.00037617 ± 0.000664 | 0.0081037 |
| $k_{ro}$ | 0.007445 ± 0.03127 | −0.035336 |
| $k_{is}$ | 0.0102506 ± 0.004418 | 0.0042311 ± 0.006932 |
| $k_{rs}$ | $3.1687 \times 10^{-6} \pm 1.455 \times 10^{-6}$ | −0.061102 ± 0.006231 |
| $k_{iso}$ | 0.00045328 ± 0.00005917 | 0.0042311 |
| $k_{rso}$ | 0.00025328 ± 0.0004963 | −0.061102 |
| $a$ | 1.8728 ± 0.2528 | |
| $b$ | 7.0396 ± 0.8488 | |
| Model 2 | | |
| $k_a$ | 0.901 | −0.079 |
| $k_d$ | 0.055 | −0.167 |
| $k_o$ | 41.126 | 0.021 |
| $k_c$ | 0.255 | 0.01 |

The table contains the estimated parameters for Model 1 (Fig. 3 A) and Model 2 (Fig. 7 A), given as mean and SD. All rate constants have the form $k = k^0 \times e^{k^1 \times V}$. The $a$ and $b$ values represent allosteric factors. SD values are not given for some of the Model 1 parameters, because those parameters were not estimated but calculated (see Materials and methods). SD values are not given for Model 2, which was truncated from Model 1 and adjusted to describe only a subset of the VC data. The voltage sensitivity factors $k^1$ can take both positive and negative values and their SDs should be interpreted as absolute values on a scale of approximately −0.15 to +0.15 mV$^{-1}$, typical of voltage-gated channels. In contrast, the SDs of the pre-exponential factors $k^0$ and allosteric factors $a$ and $b$ should be interpreted as relative to the estimated mean.

the burst, but with a clearer exponential decay (Fig. 2 F). Because the driving force is now uniform, this decay in amplitude corresponds to a decay in conductance.

According to these results, both the subthreshold and the suprathreshold $Na^+$ current components exhibit a progressive reduction in availability with each individual spike in the burst. However, the suprathreshold component reaches a steady level after fewer than 10 spikes (Fig. 2 D, middle trace), whereas the subthreshold $Na^+$ component continues to inactivate throughout the burst (Fig. 2 C), suggesting that it may require a much longer time scale—potentially, the entire interburst interval—to recover from inactivation. This reduction in the subthreshold $Na^+$ current may be responsible for the bAHP observed experimentally (Fig. 1 D). More importantly, the slow, cumulative inactivation of the subthreshold inward current may be the cause for burst termination, as it can eventually tip the balance of subthreshold currents to a point where the spike threshold cannot be reached. Furthermore, if the recovery from inactivation of the subthreshold $Na^+$ current is indeed slow, it may be responsible for the long duration of the interburst interval.

### $I_{NaP}$ recovers slowly from inactivation

To determine the rate of $I_{NaP}$ recovery from inactivation, we designed the VC pulse protocol shown in Fig. 3 A and applied it to preBötC intrinsic bursters and nonbursters. The control and test pulses (100 ms) were set at −40 mV, which we verified to be the voltage where the subthreshold $Na^+$ current exhibits maximum amplitude and can be optimally detected. This voltage also elicits a large transient inward current, which could be a mixture of $I_{NaT}$ and a space-clamp artifact (Milescu et al., 2010a). Thus, to better isolate the persistent component, we measured $I_{NaP}$ as the average current over the last 10 ms of the control or test pulses (Fig. 3 A, inset). The control and test pulses were separated by a long (1-s) inactivating pulse at +10 mV, which we found to be long enough to induce significant, although incomplete (≈50%), $I_{NaP}$ inactivation. The recovery was tested at −60 mV, which is representative for the range of membrane potentials normally experienced by preBötC cells in the interburst interval, but also at −80 mV, to characterize voltage dependence. The fraction of $I_{NaP}$ recovered from inactivation was calculated as the ratio between the persistent currents evoked by a test pulse and by the control pulse (Fig. 3 B).

Interestingly, the recovery time course of $I_{NaP}$ is biexponential (Fig. 3 B), with time constants separated by three orders of magnitude (milliseconds versus seconds), and with no significant difference between intrinsic bursters and nonbursters. Of the total $I_{NaP}$, the fraction that recovers slowly represents ∼20%. However, relative to the fraction that actually inactivates during the 1-s-long inactivating pulse (≈50%), the slow component is much larger (approximately half). Altogether, these results confirm our prediction that $I_{NaP}$ recovers very slowly from the inactivation induced by a burst, on a time scale comparable to the interburst interval (seconds). This slow increase in a small inward current may be the factor responsible for the small depolarization drift observed between bursts (Fig. 1 D, box). Even more importantly, the rate of $I_{NaP}$ recovery could control bursting frequency, because the next burst cannot be initiated and sustained until enough $I_{NaP}$ becomes available.

### Activation and inactivation properties of $I_{NaP}$

The rate of recovery from inactivation is clearly a critical property of $I_{NaP}$, but a quantitative understanding of $I_{NaP}$-dependent bursting requires additional information on $I_{NaP}$ activation and inactivation properties. The steady-state activation curve was obtained as shown in Fig. 3 C, using a depolarizing ramp protocol (33 mV/s, from −80 to −35 mV) that is slow enough to inactivate $I_{NaT}$ and leave mostly $I_{NaP}$. The current value at each voltage was first baseline-subtracted and then converted to conductance, assuming a linear current–voltage (I-V) relationship and a reversal

potential of +35 mV. Then, the entire curve was normalized to the conductance value at −40 mV and fitted with a Boltzmann equation to estimate the half-activation voltage ($V_h$) and the slope factor ($k$). The results show that $I_{NaP}$ starts to activate at ≈−70 mV and reaches a maximum at ≈−40 mV, with no significant difference between intrinsic bursters and nonbursters, in terms of $V_h$ and $k$. However, the maximum current and conductance values are approximately twice larger in bursters. This discrepancy is likely caused by a difference in conductance density, rather than cell size, as whole-cell capacitance is not significantly different between intrinsic bursters and nonbursters (Koizumi and Smith, 2008; Koizumi et al., 2013). The activation curve clearly emphasizes the subthreshold nature of $I_{NaP}$, which is turned on at more negative membrane potentials than the typical $I_{NaT}$, by as much as 25 mV. This separation allowed us to examine the time course of $I_{NaP}$ activation and deactivation at subthreshold voltages, where $I_{NaT}$ is not active. As shown in Fig. 3 D, we used voltage steps (100 ms) to activate the channel at different potentials (−60 to −50 mV) and deactivate it back to −80 mV. Both activation and deactivation have a single-exponential time course, with no significant difference in time constants between intrinsic bursters and nonbursters.

The steady-state inactivation (availability) curve was obtained as shown in Fig. 3 E, using voltage steps (1 s) to inactivate the channel at different potentials (−80 to +10 mV), followed by a slow depolarizing ramp (33 mV/s) to test availability. The peak current flowing during the ramp at −40 mV was plotted as a function of step voltage, and the entire curve was normalized to the value at −80 mV and fitted with a Boltzmann equation. The results show that $I_{NaP}$ starts to inactivate at ≈−70 mV and reaches a plateau at ≈+10 mV, with no significant difference between intrinsic bursters and nonbursters, in terms of $V_h$ and $k$. Interestingly, approximately half the current remains noninactivated at +10 mV, in agreement with the recovery from inactivation data (Fig. 3 B). It is possible that, in a limited voltage range, some of the noninactivated fraction represents contamination with the $I_{NaT}$ window current. However, we could not reliably determine this, because these neurons could not be space-clamped well enough for precise measurements of $I_{NaT}$, even with the prepulse technique (Milescu et al., 2010a).

Because $I_{NaP}$ recovers very slowly from inactivation (Fig. 3 B), we examined its inactivation time course as shown in Fig. 3 F, using long voltage steps (5 s) to activate and then inactivate the channel at different potentials (−40 to −20 mV). The response to the voltage step is a large, fast transient, followed by a slow decay to a nonzero steady-state value. Starting with the transient, the decay of the current can be explained well with a sum of three exponentials. Of these, we ascribed the slowest component to $I_{NaP}$ inactivation and used it for further analysis, excluding the first 20 ms that contain the fast transient. The results show that $I_{NaP}$ inactivates slowly (571.0 ± 50.9 ms at −40 mV), reaching a plateau at approximately half the initial value, in agreement with the steady-state inactivation curve (Fig. 3 E), with no significant difference in the time constant of decay between intrinsic bursters and nonbursters. However, in agreement with the steady-state activation curve (Fig. 3 C), the overall $I_{NaP}$ current is approximately twice larger in the intrinsic bursters. Overall, these data clearly demonstrate the persistence of $I_{NaP}$ at suprathreshold potentials, where, despite inactivation, a large fraction remains active.

### A data-derived model of $I_{NaP}$

Our next step was to assemble the results presented above into a kinetic model that we could then use in DC experiments to test the role of $I_{NaP}$ in bursting. Our goal was to construct a model that captures only the $I_{NaP}$ component of the total TTX-sensitive $Na^+$ current. Consequently, this model would not have to predict the large transient component but only the subthreshold persistent current. To formulate a model, we were guided by the experimental data shown in Fig. 3, which indicate that $I_{NaP}$ has voltage-dependent steady-state activation and inactivation, fast activation and deactivation kinetics, slow inactivation, and biexponential recovery from inactivation. Altogether, these kinetic properties are qualitatively similar to those exhibited by the TTX-sensitive $Na^+$ current previously recorded and characterized by us in raphe serotonergic neurons (Milescu et al., 2010b), with the quantitative difference that $I_{NaP}$ in preBötC neurons has slow inactivation (seconds), whereas the $Na^+$ current in serotonergic neurons has fast inactivation (milliseconds). Thus, we chose the Markov state model shown in Fig. 4 A (Model 1), with the expectation that it has enough structural flexibility to explain our $I_{NaP}$ data. Like our older model, Model 1 is based on a topology originally formulated for neuronal sodium channels (Kuo and Bean, 1994) and later expanded to explain resurgence (Raman and Bean, 2001) and long-term inactivation (Dover et al., 2010; Milescu et al., 2010b).

The kinetic parameters of Model 1 were optimized to fit the experimental data shown in Fig. 4 (B–E), as explained in Materials and methods. The solution is given in Table 1. The relatively low standard deviation values indicate that most of these parameters are well defined. As expected, the preexponential parameters that reflect slow transitions that are generally less well represented in the experimental data, such as $k_{ro}$, are also less well defined. The resulting model explains well a comprehensive set of data, including the incomplete steady-state inactivation and the biexponential recovery from inactivation. Importantly, the model also predicts well the subthreshold $Na^+$ current evoked by the realistic burst waveform (Fig. 4 F), which was calculated but not included in the fit. Like the real $Na^+$ current, the predicted current exhibits a similar reduction in amplitude throughout the burst.

### Testing $I_{NaP}$ Model 1 in computer simulations

Before using it in DC experiments, we first tested whether Model 1 is capable of sustaining oscillatory bursting behavior in previously developed and well-characterized single-compartment computational models of preBötC intrinsic bursters (Butera et al., 1999a,b), as described in Materials and methods. As shown by the simulations presented in Fig. 5, Model 1 is perfectly capable of generating voltage-dependent intrinsic oscillatory bursting, where burst initiation and termination can be effectively orchestrated by the voltage-dependent kinetic properties encapsulated in our $I_{NaP}$ model.

At the beginning of a burst, the availability (Fig. 5 A, bottom graph, red trace) reaches a maximum value that depends on

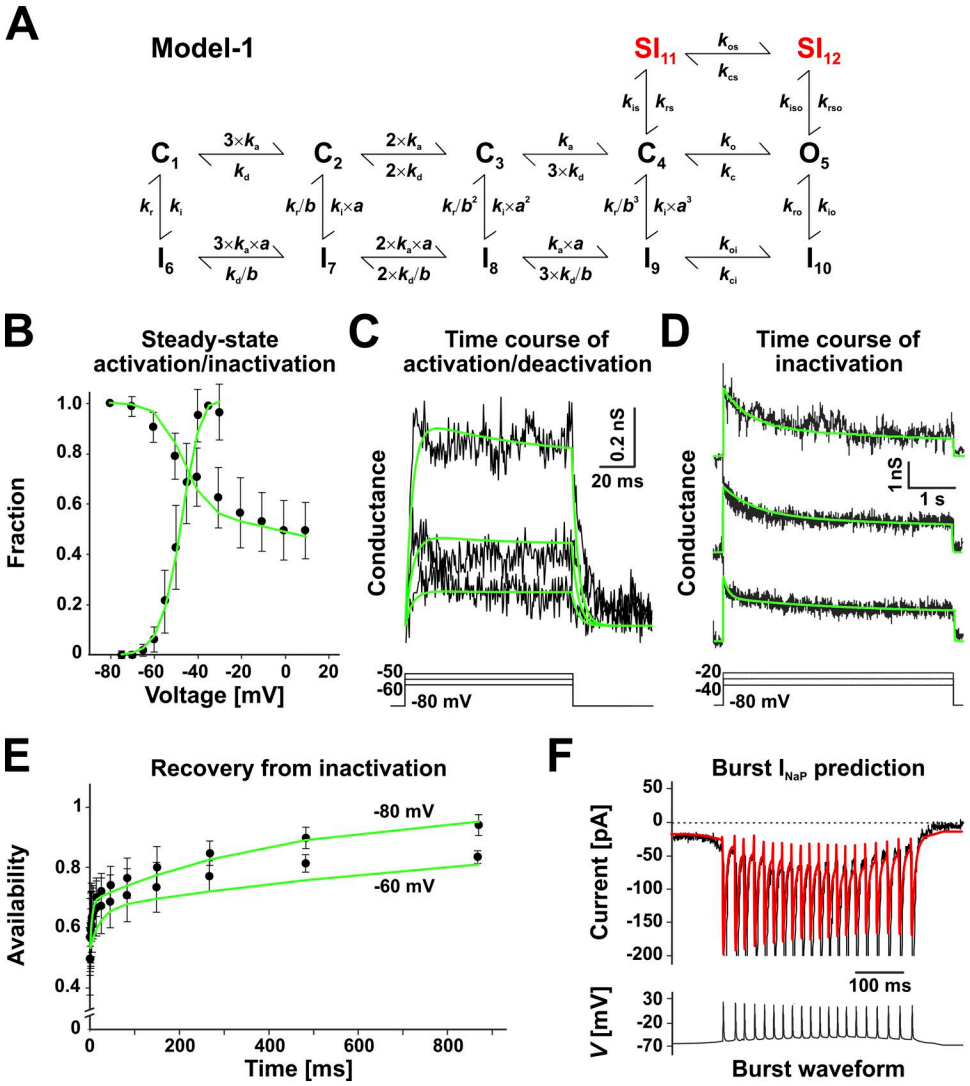


Figure 4. **A data-derived model of $I_{NaP}$ (Model 1). (A)** Markov state model optimized to simultaneously fit the experimental data in B–E (see Materials and methods). The closed states $C_1$–$C_4$, the open state $O_5$, and the inactivated states $I_6$–$I_{10}$ represent the fast activation and inactivation pathways, whereas the two inactivated states $SI_{11}$ and $SI_{12}$ create an alternative, slower inactivation pathway. The *k* parameters represent voltage-dependent microscopic rate constants, and *a* and *b* represent allosteric parameters. All rates are voltage dependent. **(B–F)** Experimental data (black traces and symbols), as described in Fig. 3 (B–E) and Fig. 2 C (F), and best-fit model predictions (green lines). The traces in C and D were obtained by converting current to conductance, assuming a reversal potential of +35 mV. In D, the initial 20 ms containing the transient were excluded from the fit. The data in F were not part of the fit, and the red waveform represents the prediction of the optimized model. The predicted current drops in amplitude during each action potential in the burst, as caused by the corresponding drop in driving force. In the experimental data, this effect is masked by the much larger $I_{NaT}$. Data shown in B and E are mean ± SD.

bursting frequency, which can be controlled via the applied current ($I_{app}$ in Fig. 5 A, top trace). In this case, we defined "availability" as the fraction of channels that, on the burst time scale, are not "frozen" in the long-lived, slow-inactivation $SI_{11}$ or $SI_{12}$ states, and are thus available to conduct current. The availability decays throughout the burst and then recovers in the interburst interval, controlling the amount of $I_{NaP}$ that can terminate a burst and initiate the next one, respectively. The decay and recovery proceed with different time constants at their respective membrane potentials, explaining the shorter bursts (less than a second) and longer interburst intervals (seconds). Overall, the simulated data match two experimentally observed key features: the bAHP and the slow depolarization drift in the interburst interval. Importantly, the simulations also confirm that bursting frequency can be tuned by shifting baseline voltage with applied current, a characteristic feature of preBötC intrinsic bursters (Fig. 1 C).

### Testing $I_{NaP}$ Model 1 in live neurons via DC

The previous test validates our $I_{NaP}$ model in computer simulations of preBötC intrinsic bursters. Clearly, the $I_{NaP}$ model establishes robust bursting in a reduced cellular model. However, the final verification is in live cells, where $I_{NaP}$ must interact appropriately with a complex battery of insufficiently characterized currents, of which $I_{NaT}$ is a prime example. Ideally, this verification would involve pharmacological block of $I_{NaP}$, followed by introduction of a model-based current, via DC (Milescu et al., 2010b). Because a completely specific blocker of $I_{NaP}$ does not exist, we adopted a different strategy that takes advantage

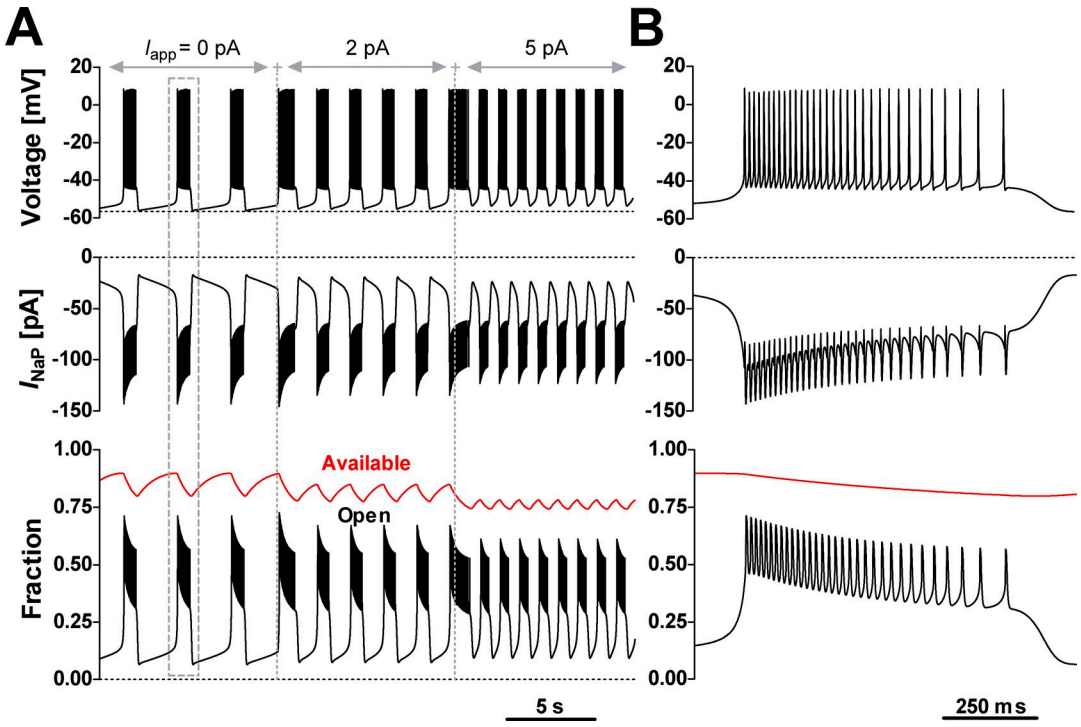


Figure 5. **$I_{NaP}$ Model 1 supports voltage-dependent rhythmic bursting in computer simulations.** The $I_{NaP}$ model was tested in a single-compartment neuronal model that also includes spike-generating and -terminating $Na^+$ and $K^+$ currents, and a $K^+$-dominated leak (see Materials and methods for details). A bias current ($I_{app}$) was applied to test bursting activity at different baseline voltages. **(A)** Time course of membrane potential (upper trace), $I_{NaP}$ (middle trace), and the fractions of $I_{NaP}$ channels residing in the open state (bottom graph, black trace) and available to conduct current (bottom graph, red trace). Availability was calculated as the sum occupancy of all states other than $SI_{11}$ and $SI_{12}$. **(B)** Expanded view of a single burst (dashed box in A). The simulations exhibit the bAHP, the depolarization drift in the interburst interval, and the voltage-dependent bursting frequency characteristic of preBötC intrinsic burster neurons (Fig. 1 D).

of the physiological differences between intrinsic bursters and nonbursters. Thus, as shown by our experiments here, $I_{NaP}$ is expressed at twice greater densities in intrinsic bursters, relative to nonbursters, but its kinetic properties seem to be similar between the two subtypes (Fig. 3). Furthermore, it has been shown that the voltage-dependent bursting behavior of neonatal rat preBötC intrinsic bursters (Del Negro et al., 2002; Koizumi et al., 2013) can be abolished with pharmacological agents that, although not very specific, reduce $I_{NaP}$ (Song et al., 1997; Koizumi and Smith, 2008). Therefore, one would expect that subtracting enough $I_{NaP}$ from preBötC intrinsic bursters, via DC, would eliminate bursting. Conversely, adding enough $I_{NaP}$ to nonbursters would instate rhythmic bursting.

First, we tested $I_{NaP}$ injection with DC into nonbursters. As illustrated in Fig. 6 A, a preBötC nonburster is typically silent or fires isolated action potentials (not present in this example) but can switch to a mode of sustained firing upon sufficient depolarization (not depicted). However, with moderate levels of injected $I_{NaP}$ ($G_{NaP}$ = 1 nS), some clusters of action potentials and transient, small-amplitude depolarizations emerge (Fig. 6 B, top two traces). Increasing the injected $G_{NaP}$ to 1.3 nS, which fully accounts for the measured difference in conductance between intrinsic bursters and nonbursters (average of 1.2 nS), instated robust oscillatory bursting in all tested neurons ($n$ = 24; Fig. 6 B, bottom two traces). Overall, these induced bursters behave very similarly to intrinsic bursters, exhibiting the characteristic bAHP and slow depolarization drift in the interburst interval (see Fig. 1 D), as well as voltage-dependent bursting frequency under injected bias current (Fig. 6 C). No significant differences were observed between intrinsic bursters and Model 1–induced bursters in terms of bursting frequency, burst duration, and bAHP, as summarized in Table 2. However, the induced bursts exhibit significantly lower action potential count and intraburst spike intervals.

Next, we tested $I_{NaP}$ subtraction from intrinsic bursters. The maximum $I_{NaP}$ conductance ($G_{NaP}$) that was subtracted was based on the measured difference in conductance between intrinsic bursters and nonbursters (see Fig. 3 C). As predicted, subtracting a Model 1–based $I_{NaP}$ from preBötC intrinsic bursters via DC stopped spontaneous bursting. An example is shown in Fig. 6 (D and E), before and during $I_{NaP}$ subtraction, respectively. Because the $I_{NaP}$ subtraction also caused a small membrane hyperpolarization (2–3 mV), we tested whether compensating for it with a depolarizing bias current can restore bursting. As shown in Fig. 6 E, this procedure could not reinstate oscillatory bursting at any baseline voltage, in any of the intrinsic bursters tested ($n$ = 7). However, when enough bias current was applied, the depolarization eventually induced repetitive spiking (Fig. 6 E). This result clearly demonstrates that subtracting $I_{NaP}$ via DC eliminates the intrinsic ability of these neurons to generate oscillatory bursting but does not interfere with their ability to generate individual spikes.

### $I_{NaP}$ slow inactivation properties play a critical role in bursting

The previous results clearly demonstrate that $I_{NaP}$ plays a critical role in the oscillatory bursting activity of preBötC inspiratory neu-

Table 2. **Bursting statistics: Comparison between preBötC intrinsic bursters and Model 1-induced bursters**

| Neuron type | Burst frequency (Hz) | bAHP amplitude (mV) | Burst duration (ms) | Action potential count | Spike interval (ms) |
|---|---|---|---|---|---|
| Model 1–induced bursters ($n$ = 24) | 0.22 ± 0.09 | 2.3 ± 0.5 | 516.3 ± 104.5 | 16.7 ± 3.7 | 33.6 ± 5.7 |
| Natural bursters ($n$ = 22) | 0.21 ± 0.07 | 2.7 ± 1.4 | 452.1 ± 144.2 | 20.4 ± 5.6 | 23.7 ± 5.4 |
| P value | 0.36 | 0.17 | 0.098 | 0.006 | 0.0001 |

The recordings were obtained as described in Fig. 1 E (intrinsic bursters; $n$ = 22) and Fig. 6 B (induced bursters; $n$ = 24). The values were calculated by averaging over five consecutive bursts in each neuron. For induced bursters, the average $G_{NaP}$ value that was required to induce rhythmic bursting with at least five action potentials per burst was 1.4 ± 0.7 nS (range: 0.5–2.7 nS). The data are mean ± SD.

rons. In a final experiment, we tested the role of slow inactivation and recovery from inactivation, which could be key properties of $I_{NaP}$ that can terminate the burst, as well as control the interburst interval, as suggested by the simulation results in Fig. 5. For this, we created Model 2 (Fig. 7 A), which has the same activation pathway as Model 1 but completely lacks inactivation. Note that the I inactivated states contribute a little to slow inactivation in Model 1, and thus were removed together with the SI states. The parameters of this model were adjusted to match the steady-state activation curve (Fig. 7 B) and the time course of activation and deactivation (Fig. 7 C), which the model explains reasonably well.

Without inactivation, we would expect Model 2 to act as a nonlinear, voltage-dependent, depolarizing conductance. It should be perfectly capable of causing a neuron to switch from silence to a pattern of sustained firing riding on top of a burst-like depolarization, but once started, it should not be able to terminate it. We tested this hypothesis by injecting $I_{NaP}$ into nonbursters, first with Model 1 to determine the $G_{NaP}$ value necessary to establish robust induced bursting behavior, then with Model 2. Because it lacks inactivation, Model 2 has a maximum open probability ≈30% greater than that of Model 1. Therefore, to ensure similar levels of maximum injected $I_{NaP}$ between the two models, $G_{NaP}$ was lowered accordingly when switching to Model 2.

As illustrated in Fig. 8, switching from Model 1 ($G_{NaP}$ = 1.3 nS) to Model 2 ($G_{NaP}$ = 1.0 nS), in the same cell, marks the transition from the typical induced rhythmic bursting (Fig. 8 A) to a dramatically different firing pattern, characterized by seemingly stochastic transitions between an active phase of sustained firing and a silent phase (Fig. 8 B). As summarized in Fig. 8 C, the bursts generated with Model 1 have a reduced duration compared with the sustained firing episodes ("on" intervals) induced by Model 2, which last an order of magnitude longer and are more variable in length. In contrast, the silent phase ("off" intervals) generated by Model 2 is substantially shorter and features a reduced bAHP compared with Model 1. Overall, these results confirm our hypothesis that the slow inactivation and slow recovery from inactivation of $I_{NaP}$ are the key factors that control burst termination and bursting frequency.

## Discussion

### $I_{NaP}$ orchestrates rhythmic bursting

According to our results, $I_{NaP}$ can regulate all essential aspects of intrinsic bursting in preBötC neurons. It does so via a simple set of kinetic properties: activation at subthreshold membrane potentials, persistence at suprathreshold potentials, and slow, voltage-dependent inactivation and recovery from inactivation (Fig. 3). Ignoring for a moment the slow inactivation and recovery, the subthreshold activation and suprathreshold persistence are two properties that effectively allow $I_{NaP}$ to institute two firing modes: quiescence, when $I_{NaP}$ is turned off, and sustained firing, when $I_{NaP}$ is on. When $I_{NaP}$ is off, the main current flowing is a $K^+$-dominated leak, which holds the membrane potential at a value below the spiking threshold. When $I_{NaP}$ is on, it supplies inward current that depolarizes the membrane to a value above the spiking threshold. In principle, as long as $I_{NaP}$ maintains its activation state (off or on), the cell will also maintain its firing mode (quiescence or sustained firing, respectively). This scenario is captured by the experiment shown in Fig. 8, where Model 2, which lacks inactivation properties, is injected into nonbursters via DC. In this case, $I_{NaP}$ is turned on and off randomly by the inevitable fluctuations in membrane potential, resulting in random transitions between quiescence and sustained firing. However, this random firing pattern should not be equated with rhythmic bursting.

To establish oscillatory bursting, an additional mechanism is required to rhythmically alternate, in a deterministic fashion, between sustained firing and quiescence. This mechanism is implemented via two key $I_{NaP}$ properties: slow inactivation (Fig. 3 F) and slow recovery from inactivation (Fig. 3 B). In this context, "slow" is in reference to the burst and interburst intervals, which are both very long (0.5–5 s) relative to a single action potential (milliseconds). Interestingly, the time constant of slow inactivation is ≈600 ms, whereas the slow component of recovery has a time constant of 2.6 s, values that match the burst and the interburst intervals, respectively. Considering Model 1 (Fig. 4 A), the slow inactivation is represented by accumulation of channels into the long-lived $SI_{l1}$ and $SI_{l2}$ states, whereas the slow recovery corresponds to the reverse process. Importantly, this slow process is voltage dependent, favoring inactivation at the more positive membrane potentials of the burst active phase and recovery from inactivation at the more negative potentials of the interburst interval. Obviously, channels that are frozen into the $SI_{l1}$ and $SI_{l2}$ states cannot conduct current. Thus, the slow inactivation provides the off-switch that turns $I_{NaP}$ off and terminates a burst, whereas the slow recovery from inactivation is the on-switch that initiates a burst. Both these switches are gradual, rather than instantaneous, and are on a "timer."

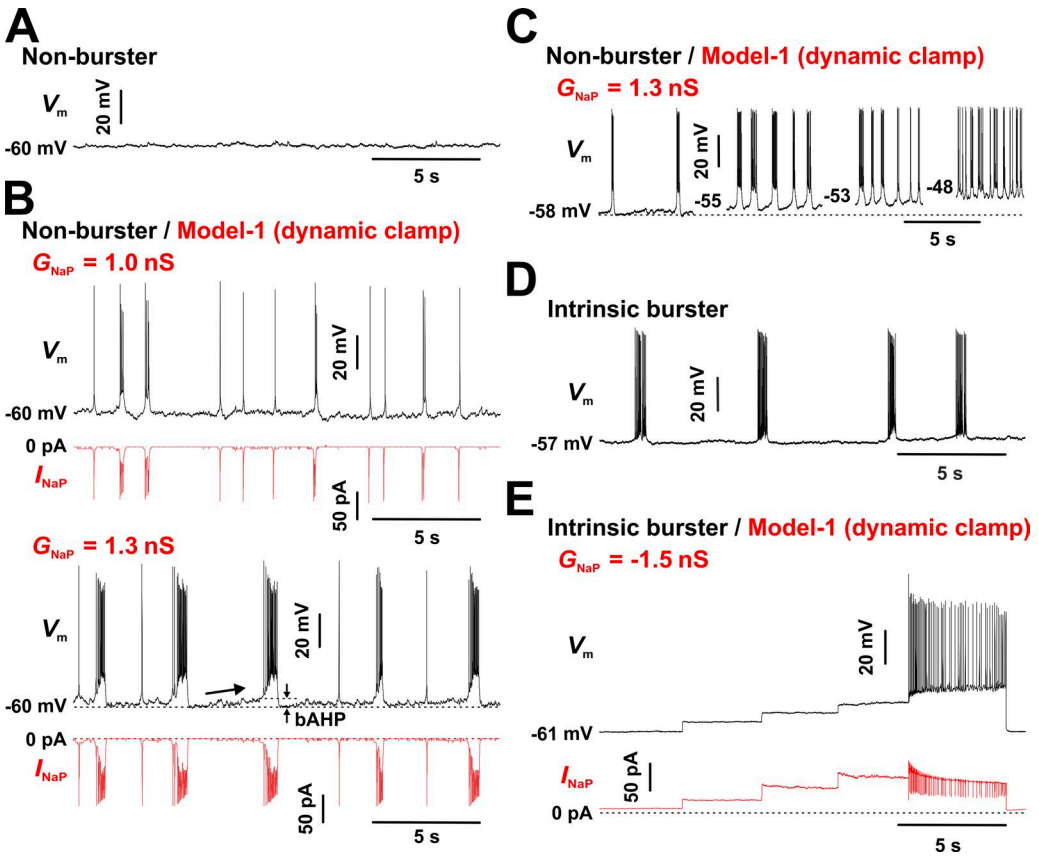


Figure 6. **Interconversion of intrinsic bursters and nonbursters by $I_{NaP}$ injection via DC.** $I_{NaP}$ predicted by Model 1 was added to nonbursters ($G_{NaP} > 0$) or subtracted from bursters ($G_{NaP} < 0$) via DC. The recordings were obtained under bath-applied $Cd^{2+}$ (200 µM) and CNQX (20 µM). **(A)** CC recording from a representative nonburster. The neuron was verified to fire repetitively when sufficiently depolarized by injecting bias current (not depicted). **(B)** Same cell as in A, but with $I_{NaP}$ added. When sufficient $I_{NaP}$ is injected ($G_{NaP}$ = 1.3 nS), the neuron exhibits robust bursting, with the bAHP and the interburst depolarization drift (arrow) characteristic of intrinsic bursters (Fig. 1 D). **(C)** Bursting frequency depends on baseline membrane potential (changed via depolarizing bias current, not depicted), a behavior typical of intrinsic bursters. A similar outcome was observed in all tested neurons ($n$ = 24). The statistics for measured parameters characterizing oscillatory bursting are given in Table 2. **(D)** CC recording from a representative intrinsic burster. The neuron was verified to have the typical voltage-dependent bursting frequency (data not shown), as illustrated in Fig. 1 D. **(E)** Same cell as in D, but with $I_{NaP}$ subtracted. The step changes in membrane potential $V_m$ and $I_{NaP}$ reflect depolarizing bias current steps of 5–10 pA. $I_{NaP}$ subtraction eliminates the ability to generate bursting activity, but the neuron can fire repetitively when sufficiently depolarized. A similar outcome was observed in all tested neurons ($n$ = 7).

During the burst, the slow inactivation caused by the overall plateau depolarization and by each action potential gradually reduces the fraction of $I_{NaP}$ able to provide depolarizing current (Fig. 5). When too much $I_{NaP}$ becomes unavailable, hyperpolarizing currents prevail and the burst terminates. There is now less subthreshold $I_{NaP}$ available, causing a bAHP. Conversely, during the interburst interval, the slow $I_{NaP}$ recovery from inactivation gradually changes the balance of net subthreshold current, creating a slow depolarization drift. When enough $I_{NaP}$ has recovered, the membrane can escape the clamping effect of leak channels, and a new burst is initiated. Because these processes are voltage dependent, it is possible to have on- and off-switches with different timing characteristics, as they occur in different voltage ranges. As a first-order approximation, the time constant of slow inactivation (hundreds of milliseconds) is the parameter that controls burst duration, whereas the time constant of recovery from inactivation (seconds) controls the interburst interval. An additional control parameter is the conductance, which must be large enough to allow $I_{NaP}$ to initiate and maintain a burst. However, considering that $I_{NaP}$ can inactivate only down to ≈50% (Fig. 3 E), the conductance cannot be too large, otherwise the burst would not terminate and the neuron would keep firing.

### $I_{NaP}$ is necessary and sufficient for intrinsic bursting

Our results strongly suggest that $I_{NaP}$ is necessary and sufficient to establish intrinsic rhythmic bursting activity in preBötC neurons, in neonatal rat brainstem slice preparations. We argue that $I_{NaP}$ is necessary for bursting, for two simple reasons. First, the fraction of preBötC neurons that express $I_{NaP}$ at lower levels do not burst intrinsically. Of course, this argument is valid only if the bursters and nonbursters differ only in their relative amount of $I_{NaP}$. We do not know if this is the case, but we do remind the reader that $I_{CAN}$, a current implicated in bursting (Thoby-Brisson and Ramirez, 2001; Peña et al., 2004; Del Negro et al., 2005; Pace et al., 2007; Rubin et al., 2009; Koizumi et al., 2018), has been silenced in our experiments (Fig. 1), together with all other $Ca^{2+}$-related currents and synaptic transmission.

The second and stronger reason is that reducing $I_{NaP}$ via DC subtraction, as shown in this study, converts intrinsic bursters

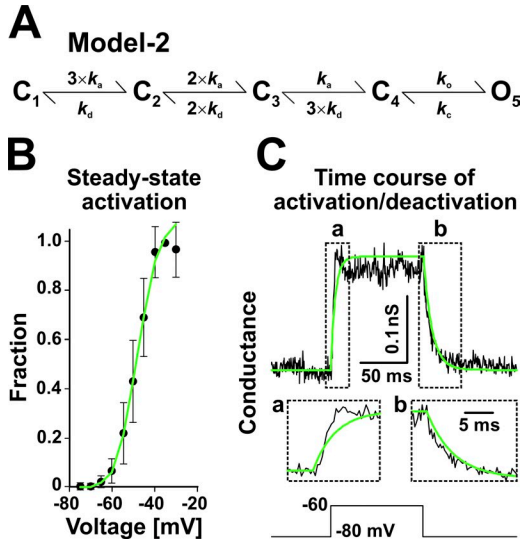


Figure 7. **A noninactivating Markov state model of $I_{NaP}$ (Model 2). (A–C)** Model (A) derived from Model 1, with all inactivated states removed and with the remaining parameters (see Materials and methods) adjusted to simultaneously fit the experimental data in B and C. The data (black traces and symbols) are as described in Fig. 4 (B and C), and the green lines represent Model 2 predictions. The data in B are mean ± SD.

into nonbursters. Certainly, the validity of this second argument is conditional on the accuracy of our $I_{NaP}$ model and the subtraction technique. However, Model 1 is based on an extensive set of VC data, which it explains well, and we have shown in the past that our DC implementation is a powerful and precise tool for testing the mechanistic contribution of ion channels to neuronal firing (Milescu et al., 2008, 2010b).

We further argue that $I_{NaP}$ is sufficient for rhythmic bursting because adding $I_{NaP}$ to nonbursters, via DC, is enough to convert them to a firing mode of rhythmic bursting that closely resembles the activity of intrinsic bursters (Table 2). Again, this is true with synaptic transmission and $Ca^{2+}$-related currents, including $I_{CAN}$, silenced. It is possible that the battery of ionic currents expressed in preBötC bursting neurons is specifically tuned for $I_{NaP}$-dependent bursting. However, the same is not necessarily true of nonbursters, which makes it even more remarkable that our $I_{NaP}$ model cooperates so well with the other currents in these cells. Furthermore, as we show here with computer simulations (Fig. 5), adding our data-derived $I_{NaP}$ model to a very simple computational neuronal model is sufficient to enable intrinsic, voltage-dependent bursting.

### $I_{NaP}$ kinetic model

The Markov model developed here (Model 1) explains well all the kinetic properties of $I_{NaP}$ in preBötC neurons (Fig. 4), inasmuch as $I_{NaP}$ could be isolated from the $I_{NaT}$ and all the other currents in the cell. However, we reemphasize that this model is not meant to describe the whole kinetic mechanism of a distinct channel (Aldrich et al., 1983), but rather a subset of kinetic features of the Nav channels expressed in preBötC neurons. Nevertheless, we based Model 1 on an allosteric model previously developed for Nav channels in mammalian neurons (Kuo and Bean, 1994; Taddese and Bean, 2002), with the difference that we shortened the activation pathway and added two additional inactivated states, $SI_{11}$ and $SI_{12}$. As noted earlier, these two states are critical features that allowed us to explain the incomplete steady-state inactivation and the two components in the time course of recovery from inactivation.

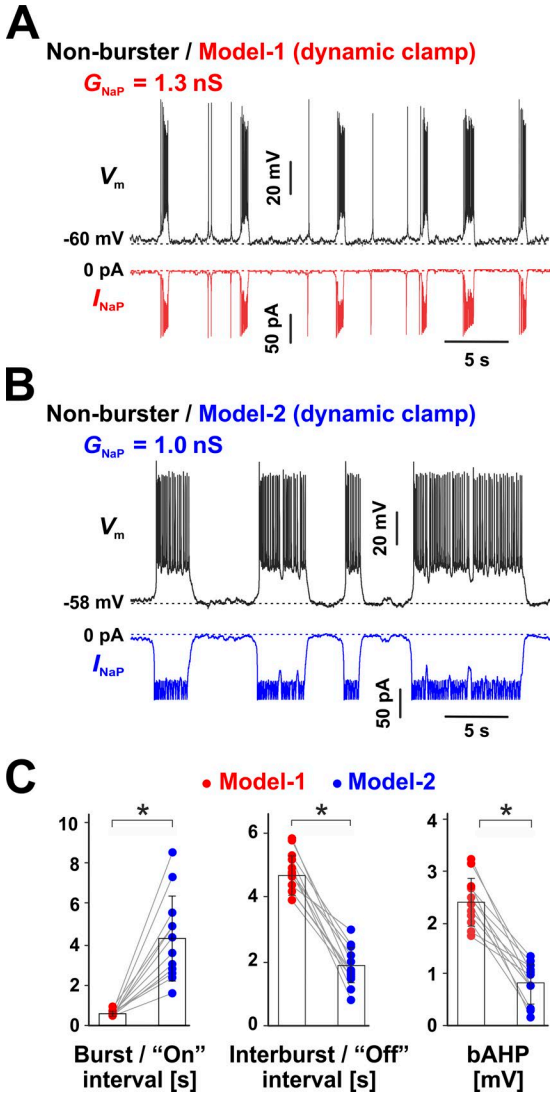


Figure 8. **$I_{NaP}$ slow inactivation and slow recovery from inactivation are required for oscillatory bursting. (A and B)** $I_{NaP}$ was added to preBötC nonbursters via DC by injecting the conductance ($G_{NaP}$) predicted by Model 1 (A) or Model 2 (B). The recordings were obtained under bath-applied $Cd^{2+}$ (200 µM) and CNQX (20 µM). **(A)** CC recording from a representative neuron, with $I_{NaP}$ generated by Model 1. The neuron exhibits robust bursting activity, similar to intrinsic bursters. **(B)** Same cell as in A but with $I_{NaP}$ generated by Model 2. The difference in $G_{NaP}$ accounts for the difference in maximum availability between the two models. The neuron now exhibits bimodal activity, with random transitions between sustained firing and quiescence. There are no isolated action potentials during the silent phase, as observed with Model 1 (A), and the bAHP and the gradual interburst depolarization are virtually absent. **(C)** Statistical comparison between Model 1– and Model 2–induced firing patterns within the same cell. The "on" interval refers to the burst (514.2 ± 89.6 ms) or sustained firing (4,257.6 ± 2,109.3 ms) duration, whereas the "off" interval refers to the interburst (4,774.7 ± 618.0 ms) or quiescent (1,927.6 ± 523.2 ms) interval, for Model 1 or Model 2, respectively. The bAHP is 2.4 ± 0.5 mV for Model 1 and 0.81 ± 0.4 mV for Model 2. All three parameters are significantly different between the two models ($n$ = 12, paired $t$; on interval, P = 0.00075; off interval, P = 0.00012; bAHP, P = 0.000021). The data in C are mean ± SD.

Why not make a comprehensive Nav model that explains both the transient and the persistent components, and use that model in DC experiments? We initially pursued this idea but found that the preBötC cells cannot be space-clamped effectively in the brain slice preparation, even with the prepulse technique (Milescu et al., 2010a), which makes it difficult to describe with enough precision the fast, transient currents. In contrast, the much slower persistent current can be well isolated and resolved. Furthermore, having a separate model for $I_{NaP}$ is actually convenient. By isolating and characterizing the persistent component, we can easily design DC experiments or simulations to test how different $I_{NaP}$ properties contribute to neuronal firing, as we have done here. In contrast, a larger, more comprehensive Nav model would be more difficult to tweak, to test hypotheses.

How applicable is our model to experimental results from kinetic analyses of $I_{NaP}$ in other neurons? Overall, the kinetic properties of $I_{NaP}$ shown here are consistent with previous studies conducted in various types of neurons (French et al., 1990; Fleidervish et al., 1996; Kay et al., 1998; Magistretti and Alonso, 1999; Aracri et al., 2006; Magistretti et al., 2006; van Drongelen et al., 2006; Carter et al., 2012; Park et al., 2013). The rather surprising incomplete steady-state inactivation (Fig. 3 E) appears to be a consistent observation (French et al., 1990; Fleidervish et al., 1996; Kay et al., 1998; Aracri et al., 2006), although some neurons show complete $I_{NaP}$ inactivation after a conditioning pulse of 10–15 s (Magistretti and Alonso, 1999; van Drongelen et al., 2006). The slow recovery from inactivation of $I_{NaP}$ has also been demonstrated, using depolarizing ramp protocols (Fleidervish et al., 1996; Magistretti and Alonso, 1999; Aracri et al., 2006; Carter et al., 2012). However, we are not aware of any study that captured both the slow and the fast components of recovery from inactivation, as we have done here.

Interestingly, the biexponential recovery of $I_{NaP}$ is reminiscent of the long-term inactivation (LTI) property of Nav channels, which has been described in various experiments from multiple neuronal types (Colbert et al., 1997; Jung et al., 1997; Mickus et al., 1999; Milescu et al., 2010b; Venkatesan et al., 2014) and has been explained as the open-state block caused by a regulatory factor (Goetz et al., 2009; Dover et al., 2010). LTI can be modeled well by connecting an additional inactivated state to the open state (Goldfarb et al., 2007; Dover et al., 2010; Milescu et al., 2010b), similar to what we have done here with the SI states in Model 1. Accumulation into this inactivated state is fast (milliseconds) during the brief depolarization of an action potential, whereas depletion is slow (hundreds of milliseconds) when the membrane is hyperpolarized during the interspike interval. In raphe serotonergic neurons, for example, the LTI mechanism establishes a pattern of spontaneous spiking at low frequencies (1–5 Hz), by regulating the amount of subthreshold Nav current that controls the spiking frequency (Milescu et al., 2010b). Although the preBötC bursters implement a very different firing pattern, they also rely on the slow recovery from inactivation of a subthreshold current, individually described here as $I_{NaP}$, to regulate their very slow bursting activity (0.1–0.5 Hz).

### Physiological implications

The preBötC contains essential circuits for generating the normal respiratory rhythm, as well as gasping, which is a vital resuscitation mode of respiratory rhythm in response to hypoxia. These functions are blunted in vivo by targeted deletions (Gray et al., 2001; Wenninger et al., 2004; McKay and Feldman, 2008) or in vitro by pharmacological manipulation (Tryba et al., 2006) of preBötC neurons. Rhythmogenesis has been proposed to rely on both $I_{NaP}$-dependent and $Ca^{2+}$-dependent cellular bursting mechanisms (Smith et al., 2007; Del Negro and Hayes, 2008; Rubin et al., 2009; Del Negro et al., 2010; Jasinski et al., 2013) in the isolated preBötC network in vitro, whereas in situ and in vivo studies consistently indicate that gasping relies solely on $I_{NaP}$-dependent bursting mechanisms (Aldrich et al., 1983; Ramirez et al., 2004; Paton et al., 2006; Paton and St.-John, 2007; Peña, 2008; St.-John et al., 2009). Furthermore, cellular hypoxia has been shown to augment the $I_{NaP}$ expressed in preBötC neurons (Koizumi and Smith, 2008; Fu et al., 2017), as well as in other cell types (Ju et al., 1996), thus increasing the "drive" to breathe when oxygen supply is low. The dysfunction of this gasping behavior is proposed to underlie life-critical conditions such as sudden infant death syndrome (Poets et al., 1999; Leiter and Böhm, 2007).

Our study brings a better understanding of $I_{NaP}$ kinetics and $I_{NaP}$-dependent bursting, which play central roles in these vital brain functions. At the molecular level, we now have a data-based, quantitative description of the kinetic properties of $I_{NaP}$, a current not only critical for respiratory-related bursting activity, but also responsible for shaping the firing patterns of many types of neurons. At the cellular level, we have advanced our understanding of the quantitative relationships between the properties of $I_{NaP}$ and the mechanism of oscillatory bursting in preBötC respiratory neurons. $I_{NaP}$ is ubiquitously expressed among these neurons, in both intrinsic bursters and nonbursters (Del Negro et al., 2002; Koizumi and Smith, 2008), especially within the critical excitatory glutamatergic neurons (Koizumi et al., 2013, 2016). Current models for respiratory rhythm generation incorporate $I_{NaP}$ in these preBötC excitatory neurons (e.g., Butera et al., 1999a,b; Smith et al., 2007; Rubin et al., 2009; Jasinski et al., 2013; Bacak et al., 2016), where the kinetic properties of slow inactivation and slow recovery from inactivation of $I_{NaP}$ have been assumed but not determined experimentally. We have quantified these properties here and thus have validated the fundamental premise that the slow inactivation and recovery from inactivation of $I_{NaP}$ play a basic role in establishing oscillatory bursting.

Finally, at the network level, we have a better understanding of the molecular factors that could control the activity of circuits in the preBötC. Importantly, we show that the amount of $I_{NaP}$ in bursters is about twice as large as in nonbursters, but the kinetic properties of $I_{NaP}$ are similar between the two populations. Thus, if preBötC network activity is shaped by the fraction of intrinsic bursters (Purvis et al., 2007; Rybak et al., 2014), the network could be efficiently regulated via the $I_{NaP}$ amplitude, which appears to be the key factor that determines the intrinsic bursting capability. Furthermore, even though nonbursters lack sufficient $I_{NaP}$ to intrinsically initiate burst firing, the $I_{NaP}$ inactivation and recovery properties may nonetheless influence their bursting

behavior by promoting burst synchronization and termination when these cells are driven by synaptic inputs. Indeed, these cellular-level voltage-dependent properties of $I_{NaP}$ are proposed to enable multiple rhythmogenic mechanisms and their dynamic features at the network level (e.g., Smith et al., 2007; Rubin et al., 2009). Accordingly, $I_{NaP}$ may play yet another important role in orchestrating neuron population-level oscillatory bursting, as has been theoretically demonstrated by modeling studies (Butera et al., 1999a,b; Purvis et al., 2007; Rybak et al., 2014; Bacak et al., 2016).

## Acknowledgments

We thank the members of the Milescu and Smith laboratories, especially Ruli Zhang for her assistance with the experimental procedures. We are very grateful to Mirela Milescu for her many invaluable comments and suggestions on the manuscript.

This work was supported in part by the Intramural Research Program of the National Institutes of Health, National Institute of Neurological Disorders and Stroke, by American Heart Association grant 13SDG16990083 to L.S. Milescu., and by National Institutes of Health Initiative for Maximizing Student Development Fellowship R25GM056901 to M.A. Navarro.

The authors declare no competing financial interests.

Author contributions: T. Yamanishi, H. Koizumi, M.A. Navarro, and L.S. Milescu performed experiments. J.C. Smith, L.S. Milescu, and T. Yamanishi designed experiments; T. Yamanishi, H. Koizumi, M.A. Navarro, L.S. Milescu, and J.C. Smith wrote and edited the manuscript.

Richard W. Aldrich served as editor.

Submitted: 20 April 2018
Revised: 14 August 2018
Accepted: 19 September 2018

## References

Aldrich, R.W., D.P. Corey, and C.F. Stevens. 1983. A reinterpretation of mammalian sodium channel gating based on single channel recording. *Nature.* 306:436–441. https://doi.org/10.1038/306436a0

Aman, T.K., T.M. Grieco-Calub, C. Chen, R. Rusconi, E.A. Slat, L.L. Isom, and I.M. Raman. 2009. Regulation of persistent Na current by interactions between β subunits of voltage-gated Na channels. *J. Neurosci.* 29:2027–2042. https://doi.org/10.1523/JNEUROSCI.4531-08.2009

Aracri, P., E. Colombo, M. Mantegazza, P. Scalmani, G. Curia, G. Avanzini, and S. Franceschetti. 2006. Layer-specific properties of the persistent sodium current in sensorimotor cortex. *J. Neurophysiol.* 95:3460–3468. https://doi.org/10.1152/jn.00588.2005

Attwell, D., I. Cohen, D. Eisner, M. Ohba, and C. Ojeda. 1979. The steady state TTX-sensitive ("window") sodium current in cardiac Purkinje fibres. *Pflugers Arch.* 379:137–142. https://doi.org/10.1007/BF00586939

Bacak, B.J., T. Kim, J.C. Smith, J.E. Rubin, and I.A. Rybak. 2016. Mixed-mode oscillations and population bursting in the pre-Bötzinger complex. *eLife.* 5:e13403. https://doi.org/10.7554/eLife.13403

Bant, J.S., and I.M. Raman. 2010. Control of transient, resurgent, and persistent current by open-channel block by Na channel beta4 in cultured cerebellar granule neurons. *Proc. Natl. Acad. Sci. USA.* 107:12357–12362. https://doi.org/10.1073/pnas.1005633107

Butera, R.J. Jr., J. Rinzel, and J.C. Smith. 1999a. Models of respiratory rhythm generation in the pre-Bötzinger complex. I. Bursting pacemaker neurons. *J. Neurophysiol.* 82:382–397. https://doi.org/10.1152/jn.1999.82.1.382

Butera, R.J., Jr., J. Rinzel, and J.C. Smith. 1999b. Models of respiratory rhythm generation in the pre-Bötzinger complex. II. Populations of coupled pacemaker neurons. *J. Neurophysiol.* 82:398–415. https://doi.org/10.1152/jn.1999.82.1.398

Carter, B.C., A.J. Giessel, B.L. Sabatini, and B.P. Bean. 2012. Transient sodium current at subthreshold voltages: activation by EPSP waveforms. *Neuron.* 75:1081–1093. https://doi.org/10.1016/j.neuron.2012.08.033

Chahine, M., and M.E. O'Leary. 2011. Regulatory Role of Voltage-Gated Na Channel β Subunits in Sensory Neurons. *Front. Pharmacol.* 2:70. https://doi.org/10.3389/fphar.2011.00070

Chatelier, A., J. Zhao, P. Bois, and M. Chahine. 2010. Biophysical characterisation of the persistent sodium current of the Nav1.6 neuronal sodium channel: a single-channel analysis. *Pflugers Arch.* 460:77–86. https://doi.org/10.1007/s00424-010-0801-9

Chevalier, M., R. De Sa, L. Cardoit, and M. Thoby-Brisson. 2016. Mechanisms Underlying Adaptation of Respiratory Network Activity to Modulatory Stimuli in the Mouse Embryo. *Neural Plast.* 2016:3905257. https://doi.org/10.1155/2016/3905257

Colbert, C.M., J.C. Magee, D.A. Hoffman, and D. Johnston. 1997. Slow recovery from inactivation of Na+ channels underlies the activity-dependent attenuation of dendritic action potentials in hippocampal CA1 pyramidal neurons. *J. Neurosci.* 17:6512–6521. https://doi.org/10.1523/JNEUROSCI.17-17-06512.1997

Crill, W.E. 1996. Persistent sodium current in mammalian central neurons. *Annu. Rev. Physiol.* 58:349–362. https://doi.org/10.1146/annurev.ph.58.030196.002025

Darbon, P., C. Yvon, J.C. Legrand, and J. Streit. 2004. INaP underlies intrinsic spiking and rhythm generation in networks of cultured rat spinal cord neurons. *Eur. J. Neurosci.* 20:976–988. https://doi.org/10.1111/j.1460-9568.2004.03565.x

de Hass, V., and W. Vogel. 1989. Sodium and potassium currents recorded during an action potential. *Eur. Biophys. J.* 17:49–51. https://doi.org/10.1007/BF00257145

Del Negro, C.A., and J.A. Hayes. 2008. A 'group pacemaker' mechanism for respiratory rhythm generation. *J. Physiol.* 586:2245–2246. https://doi.org/10.1113/jphysiol.2008.153627

Del Negro, C.A., S.M. Johnson, R.J. Butera, and J.C. Smith. 2001. Models of respiratory rhythm generation in the pre-Bötzinger complex. III. Experimental tests of model predictions. *J. Neurophysiol.* 86:59–74. https://doi.org/10.1152/jn.2001.86.1.59

Del Negro, C.A., N. Koshiya, R.J. Butera Jr., and J.C. Smith. 2002. Persistent sodium current, membrane properties and bursting behavior of pre-Bötzinger complex inspiratory neurons in vitro. *J. Neurophysiol.* 88:2242–2250. https://doi.org/10.1152/jn.00081.2002

Del Negro, C.A., C. Morgado-Valle, J.A. Hayes, D.D. Mackay, R.W. Pace, E.A. Crowder, and J.L. Feldman. 2005. Sodium and calcium current-mediated pacemaker neurons and respiratory rhythm generation. *J. Neurosci.* 25:446–453. https://doi.org/10.1523/JNEUROSCI.2237-04.2005

Del Negro, C.A., J.A. Hayes, R.W. Pace, B.R. Brush, R. Teruyama, and J.L. Feldman. 2010. Synaptically activated burst-generating conductances may underlie a group-pacemaker mechanism for respiratory rhythm generation in mammals. Prog. Brain Res. 187:111–136.

Do, M.T.H., and B.P. Bean. 2003. Subthreshold sodium currents and pacemaking of subthalamic neurons: modulation by slow inactivation. *Neuron.* 39:109–120. https://doi.org/10.1016/S0896-6273(03)00360-X

Dover, K., S. Solinas, E. D'Angelo, and M. Goldfarb. 2010. Long-term inactivation particle for voltage-gated sodium channels. *J. Physiol.* 588:3695–3711. https://doi.org/10.1113/jphysiol.2010.192559

Feldman, J.L., and C.A. Del Negro. 2006. Looking for inspiration: new perspectives on respiratory rhythm. *Nat. Rev. Neurosci.* 7:232–241. https://doi.org/10.1038/nrn1871

Fleidervish, I.A., A. Friedman, and M.J. Gutnick. 1996. Slow inactivation of Na+ current and slow cumulative spike adaptation in mouse and guinea-pig neocortical neurones in slices. *J. Physiol.* 493:83–97. https://doi.org/10.1113/jphysiol.1996.sp021366

French, C.R., P. Sah, K.J. Buckett, and P.W. Gage. 1990. A voltage-dependent persistent sodium current in mammalian hippocampal neurons. *J. Gen. Physiol.* 95:1139–1157. https://doi.org/10.1085/jgp.95.6.1139

Fu, C., J. Hao, M. Zeng, Y. Song, W. Jiang, P. Zhang, A. Luo, Z. Cao, L. Belardinelli, and J. Ma. 2017. Modulation of late sodium current by $Ca^{2+}$ -calmodulin-dependent protein kinase II, protein kinase C and $Ca^{2+}$ during hypoxia in rabbit ventricular myocytes. *Exp. Physiol.* 102:818–834. https://doi.org/10.1113/EP085990

Goetz, R., K. Dover, F. Laezza, N. Shtraizent, X. Huang, D. Tchetchik, A.V. Eliseenkova, C.-F. Xu, T.A. Neubert, D.M. Ornitz, et al. 2009. Crystal structure of a fibroblast growth factor homologous factor (FHF) defines a conserved surface on FHFs for binding and modulation of voltage-gated sodium channels. *J. Biol. Chem.* 284:17883–17896. https://doi.org/10.1074/jbc.M109.001842

Goldfarb, M., J. Schoorlemmer, A. Williams, S. Diwakar, Q. Wang, X. Huang, J. Giza, D. Tchetchik, K. Kelley, A. Vega, et al. 2007. Fibroblast growth factor homologous factors control neuronal excitability through modulation of voltage-gated sodium channels. *Neuron.* 55:449–463. https://doi.org/10.1016/j.neuron.2007.07.006

Gray, P.A., W.A. Janczewski, N. Mellen, D.R. McCrimmon, and J.L. Feldman. 2001. Normal breathing requires preBötzinger complex neurokinin-1 receptor-expressing neurons. *Nat. Neurosci.* 4:927–930. https://doi.org/10.1038/nn0901-927

Jackson, A.C., and B.P. Bean. 2007. State-dependent enhancement of subthreshold A-type potassium current by 4-aminopyridine in tuberomammillary nucleus neurons. *J. Neurosci.* 27:10785–10796. https://doi.org/10.1523/JNEUROSCI.0935-07.2007

Jasinski, P.E., Y.I. Molkov, N.A. Shevtsova, J.C. Smith, and I.A. Rybak. 2013. Sodium and calcium mechanisms of rhythmic bursting in excitatory neural networks of the pre-Bötzinger complex: a computational modelling study. *Eur. J. Neurosci.* 37:212–230. https://doi.org/10.1111/ejn.12042

Jensen, M.S., R. Azouz, and Y. Yaari. 1994. Variant firing patterns in rat hippocampal pyramidal cells modulated by extracellular potassium. *J. Neurophysiol.* 71:831–839. https://doi.org/10.1152/jn.1994.71.3.831

Ju, Y.-K., D.A. Saint, and P.W. Gage. 1996. Hypoxia increases persistent sodium current in rat ventricular myocytes. *J. Physiol.* 497:337–347. https://doi.org/10.1113/jphysiol.1996.sp021772

Jung, H.-Y., T. Mickus, and N. Spruston. 1997. Prolonged sodium channel inactivation contributes to dendritic action potential attenuation in hippocampal pyramidal neurons. *J. Neurosci.* 17:6639–6646. https://doi.org/10.1523/JNEUROSCI.17-17-06639.1997

Kay, A.R., M. Sugimori, and R. Llinás. 1998. Kinetic and stochastic properties of a persistent sodium current in mature guinea pig cerebellar Purkinje cells. *J. Neurophysiol.* 80:1167–1179. https://doi.org/10.1152/jn.1998.80.3.1167

Koizumi, H., and J.C. Smith. 2008. Persistent Na+ and K+-dominated leak currents contribute to respiratory rhythm generation in the pre-Bötzinger complex in vitro. *J. Neurosci.* 28:1773–1785. https://doi.org/10.1523/JNEUROSCI.3916-07.2008

Koizumi, H., N. Koshiya, J.X. Chia, F. Cao, J. Nugent, R. Zhang, and J.C. Smith. 2013. Structural-functional properties of identified excitatory and inhibitory interneurons within pre-Botzinger complex respiratory microcircuits. *J. Neurosci.* 33:2994–3009. https://doi.org/10.1523/JNEUROSCI.4427-12.2013

Koizumi, H., B. Mosher, M.F. Tariq, R. Zhang, N. Koshiya, and J.C. Smith. 2016. Voltage-dependent rhythmogenic property of respiratory pre-Bötzinger complex glutamatergic, Dbx1-derived, and somatostatin-expressing neuron populations revealed by graded optogenetic inhibition. *eNeuro.* 3:0081-0016.2016.

Koizumi, H., T.T. John, J.X. Chia, M.F. Tariq, R.S. Phillips, B. Mosher, Y. Chen, R. Thompson, R. Zhang, and N. Koshiya. 2018. Transient receptor potential channels TRPM4 and TRPC3 critically contribute to respiratory motor pattern formation but not rhythmogenesis in rodent brainstem circuits. eNeuro. 5:0332-0317.2018.

Koshiya, N., and J.C. Smith. 1999. Neuronal pacemaker for breathing visualized in vitro. *Nature.* 400:360–363. https://doi.org/10.1038/22540

Kuo, C.C., and B.P. Bean. 1994. Na+ channels must deactivate to recover from inactivation. *Neuron.* 12:819–829. https://doi.org/10.1016/0896-6273(94)90335-2

Leiter, J.C., and I. Böhm. 2007. Mechanisms of pathogenesis in the sudden infant death syndrome. *Respir. Physiol. Neurobiol.* 159:127–138. https://doi.org/10.1016/j.resp.2007.05.014

Lopez-Santiago, L.F., W.J. Brackenbury, C. Chen, and L.L. Isom. 2011. Na+ channel Scn1b gene regulates dorsal root ganglion nociceptor excitability in vivo. *J. Biol. Chem.* 286:22913–22923. https://doi.org/10.1074/jbc.M111.242370

Magistretti, J., and A. Alonso. 1999. Biophysical properties and slow voltage-dependent inactivation of a sustained sodium current in entorhinal cortex layer-II principal neurons: a whole-cell and single-channel study. *J. Gen. Physiol.* 114:491–509. https://doi.org/10.1085/jgp.114.4.491

Magistretti, J., L. Castelli, L. Forti, and E. D'Angelo. 2006. Kinetic and functional analysis of transient, persistent and resurgent sodium currents in rat cerebellar granule cells in situ: an electrophysiological and modelling study. *J. Physiol.* 573:83–106. https://doi.org/10.1113/jphysiol.2006.106682

Maurice, N., T. Tkatch, M. Meisler, L.K. Sprunger, and D.J. Surmeier. 2001. D1/D5 dopamine receptor activation differentially modulates rapidly inactivating and persistent sodium currents in prefrontal cortex pyramidal neurons. *J. Neurosci.* 21:2268–2277. https://doi.org/10.1523/JNEUROSCI.21-07-02268.2001

McKay, L.C., and J.L. Feldman. 2008. Unilateral ablation of pre-Botzinger complex disrupts breathing during sleep but not wakefulness. *Am. J. Respir. Crit. Care Med.* 178:89–95. https://doi.org/10.1164/rccm.200712-1901OC

Mickus, T., H. Jung, and N. Spruston. 1999. Properties of slow, cumulative sodium channel inactivation in rat hippocampal CA1 pyramidal neurons. *Biophys. J.* 76:846–860. https://doi.org/10.1016/S0006-3495(99)77248-6

Milescu, L.S., T. Yamanishi, K. Ptak, M.Z. Mogri, and J.C. Smith. 2008. Real-time kinetic modeling of voltage-gated ion channels using dynamic clamp. *Biophys. J.* 95:66–87. https://doi.org/10.1529/biophysj.107.118190

Milescu, L.S., B.P. Bean, and J.C. Smith. 2010a. Isolation of somatic Na+ currents by selective inactivation of axonal channels with a voltage prepulse. *J. Neurosci.* 30:7740–7748. https://doi.org/10.1523/JNEUROSCI.6136-09.2010

Milescu, L.S., T. Yamanishi, K. Ptak, and J.C. Smith. 2010b. Kinetic properties and functional dynamics of sodium channels during repetitive spiking in a slow pacemaker neuron. *J. Neurosci.* 30:12113–12127. https://doi.org/10.1523/JNEUROSCI.0445-10.2010

Navarro, M.A., A. Salari, M. Milescu, and L.S. Milescu. 2018. Estimating kinetic mechanisms with prior knowledge II: Behavioral constraints and numerical tests. *J. Gen. Physiol.* 150:339–354. https://doi.org/10.1085/jgp.201711912

Pace, R.W., D.D. Mackay, J.L. Feldman, and C.A. Del Negro. 2007. Inspiratory bursts in the preBötzinger complex depend on a calcium-activated non-specific cation current linked to glutamate receptors in neonatal mice. *J. Physiol.* 582:113–125. https://doi.org/10.1113/jphysiol.2007.133660

Pagliardini, S., J. Ren, and J.J. Greer. 2003. Ontogeny of the pre-Bötzinger complex in perinatal rats. *J. Neurosci.* 23:9575–9584. https://doi.org/10.1523/JNEUROSCI.23-29-09575.2003

Park, Y.Y., D. Johnston, and R. Gray. 2013. Slowly inactivating component of Na+ current in peri-somatic region of hippocampal CA1 pyramidal neurons. *J. Neurophysiol.* 109:1378–1390. https://doi.org/10.1152/jn.00435.2012

Paton, J.F., and W.M. St.-John. 2007. Counterpoint: Medullary pacemaker neurons are essential for gasping, but not eupnea, in mammals. *J. Appl. Physiol.* 103:718–720. https://doi.org/10.1152/japplphysiol.00003.2007a

Paton, J.F., A.P. Abdala, H. Koizumi, J.C. Smith, and W.M. St.-John. 2006. Respiratory rhythm generation during gasping depends on persistent sodium current. *Nat. Neurosci.* 9:311–313. https://doi.org/10.1038/nn1650

Peña, F. 2008. Contribution of pacemaker neurons to respiratory rhythms generation in vitro. *In* Integration in Respiratory Control. Springer, New York. 114–118. https://doi.org/10.1007/978-0-387-73693-8_20

Peña, F., M.A. Parkis, A.K. Tryba, and J.-M. Ramirez. 2004. Differential contribution of pacemaker properties to the generation of respiratory rhythms during normoxia and hypoxia. *Neuron.* 43:105–117. https://doi.org/10.1016/j.neuron.2004.06.023

Poets, C.F., R.G. Meny, M.R. Chobanian, and R.E. Bonofiglo. 1999. Gasping and other cardiorespiratory patterns during sudden infant deaths. *Pediatr. Res.* 45:350–354. https://doi.org/10.1203/00006450-199903000-00010

Purvis, L.K., J.C. Smith, H. Koizumi, and R.J. Butera. 2007. Intrinsic bursters increase the robustness of rhythm generation in an excitatory network. *J. Neurophysiol.* 97:1515–1526. https://doi.org/10.1152/jn.00908.2006

Qu, Y., R. Curtis, D. Lawson, K. Gilbride, P. Ge, P.S. DiStefano, I. Silos-Santiago, W.A. Catterall, and T. Scheuer. 2001. Differential modulation of sodium channel gating and persistent sodium currents by the β1, β2, and β3 subunits. *Mol. Cell. Neurosci.* 18:570–580. https://doi.org/10.1006/mcne.2001.1039

Raman, I.M., and B.P. Bean. 2001. Inactivation and recovery of sodium currents in cerebellar Purkinje neurons: evidence for two mechanisms. *Biophys. J.* 80:729–737. https://doi.org/10.1016/S0006-3495(01)76052-3

Raman, I.M., L.K. Sprunger, M.H. Meisler, and B.P. Bean. 1997. Altered subthreshold sodium currents and disrupted firing patterns in Purkinje neurons of Scn8a mutant mice. *Neuron.* 19:881–891. https://doi.org/10.1016/S0896-6273(00)80969-1

Ramirez, J.-M., A.K. Tryba, and F. Peña. 2004. Pacemaker neurons and neuronal networks: an integrative view. *Curr. Opin. Neurobiol.* 14:665–674. https://doi.org/10.1016/j.conb.2004.10.011

Richter, D.W., and J.C. Smith. 2014. Respiratory rhythm generation in vivo. *Physiology (Bethesda)*. 29:58–71.
Rotstein, H.G., T. Oppermann, J.A. White, and N. Kopell. 2006. The dynamic structure underlying subthreshold oscillatory activity and the onset of spikes in a model of medial entorhinal cortex stellate cells. *J. Comput. Neurosci.* 21:271–292. https://doi.org/10.1007/s10827-006-8096-8
Rubin, J.E., J.A. Hayes, J.L. Mendenhall, and C.A. Del Negro. 2009. Calcium-activated nonspecific cation current and synaptic depression promote network-dependent burst oscillations. *Proc. Natl. Acad. Sci. USA.* 106:2939–2944. https://doi.org/10.1073/pnas.0808776106
Rybak, I.A., N.A. Shevtsova, W.M. St.-John, J.F. Paton, and O. Pierrefiche. 2003. Endogenous rhythm generation in the pre-Bötzinger complex and ionic currents: modelling and in vitro studies. *Eur. J. Neurosci.* 18:239–257. https://doi.org/10.1046/j.1460-9568.2003.02739.x
Rybak, I.A., N.A. Shevtsova, K. Ptak, and D.R. McCrimmon. 2004. Intrinsic bursting activity in the pre-Bötzinger complex: role of persistent sodium and potassium currents. *Biol. Cybern.* 90:59–74. https://doi.org/10.1007/s00422-003-0447-1
Rybak, I.A., Y.I. Molkov, P.E. Jasinski, N.A. Shevtsova, and J.C. Smith. 2014. Rhythmic bursting in the pre-Bötzinger complex: mechanisms and models. Prog. Brain Res. 209:1–23.
Salari, A., M.A. Navarro, and L.S. Milescu. 2016. Modeling the kinetic mechanisms of voltage-gated ion channels. *In* Advanced Patch-Clamp Analysis for Neuroscientists. Neuromethods. Vol. 113. A. Korngreen, editor. Humana Press, New York. https://doi.org/10.1007/978-1-4939-3411-9_13
Salari, A., M.A. Navarro, M. Milescu, and L.S. Milescu. 2018. Estimating kinetic mechanisms with prior knowledge I: Linear parameter constraints. *J. Gen. Physiol.* 150:323–338. https://doi.org/10.1085/jgp.201711911
Sanhueza, M., and J. Bacigalupo. 2005. Intrinsic subthreshold oscillations of the membrane potential in pyramidal neurons of the olfactory amygdala. *Eur. J. Neurosci.* 22:1618–1626. https://doi.org/10.1111/j.1460-9568.2005.04341.x
Sharp, A.A., M.B. O'Neil, L.F. Abbott, and E. Marder. 1993. Dynamic clamp: computer-generated conductances in real neurons. *J. Neurophysiol.* 69:992–995. https://doi.org/10.1152/jn.1993.69.3.992
Smith, J.C., H.H. Ellenberger, K. Ballanyi, D.W. Richter, and J.L. Feldman. 1991. Pre-Bötzinger complex: a brainstem region that may generate respiratory rhythm in mammals. *Science.* 254:726–729. https://doi.org/10.1126/science.1683005
Smith, J.C., A.P. Abdala, H. Koizumi, I.A. Rybak, and J.F. Paton. 2007. Spatial and functional architecture of the mammalian brain stem respiratory network: a hierarchy of three oscillatory mechanisms. *J. Neurophysiol.* 98:3370–3387. https://doi.org/10.1152/jn.00985.2007
Song, J.-H., C.-S. Huang, K. Nagata, J.Z. Yeh, and T. Narahashi. 1997. Differential action of riluzole on tetrodotoxin-sensitive and tetrodotoxin-resistant sodium channels. *J. Pharmacol. Exp. Ther.* 282:707–714.
St.-John, W.M., R.L. Stornetta, P.G. Guyenet, and J.F. Paton. 2009. Location and properties of respiratory neurones with putative intrinsic bursting properties in the rat in situ. *J. Physiol.* 587:3175–3188. https://doi.org/10.1113/jphysiol.2009.170308
Taddese, A., and B.P. Bean. 2002. Subthreshold sodium current from rapidly inactivating sodium channels drives spontaneous firing of tuberomammillary neurons. *Neuron.* 33:587–600. https://doi.org/10.1016/S0896-6273(02)00574-3
Tazerart, S., J.-C. Viemari, P. Darbon, L. Vinay, and F. Brocard. 2007. Contribution of persistent sodium current to locomotor pattern generation in neonatal rats. *J. Neurophysiol.* 98:613–628. https://doi.org/10.1152/jn.00316.2007
Thoby-Brisson, M., and J.-M. Ramirez. 2001. Identification of two types of inspiratory pacemaker neurons in the isolated respiratory neural network of mice. *J. Neurophysiol.* 86:104–112. https://doi.org/10.1152/jn.2001.86.1.104
Tryba, A.K., F. Peña, and J.-M. Ramirez. 2003. Stabilization of bursting in respiratory pacemaker neurons. *J. Neurosci.* 23:3538–3546. https://doi.org/10.1523/JNEUROSCI.23-08-03538.2003
Tryba, A.K., F. Peña, and J.-M. Ramirez. 2006. Gasping activity in vitro: a rhythm dependent on 5-HT2A receptors. *J. Neurosci.* 26:2623–2634. https://doi.org/10.1523/JNEUROSCI.4186-05.2006
Urbani, A., and O. Belluzzi. 2000. Riluzole inhibits the persistent sodium current in mammalian CNS neurons. *Eur. J. Neurosci.* 12:3567–3574. https://doi.org/10.1046/j.1460-9568.2000.00242.x
van Drongelen, W., H. Koch, F.P. Elsen, H.C. Lee, A. Mrejeru, E. Doren, C.J. Marcuccilli, M. Hereld, R.L. Stevens, and J.-M. Ramirez. 2006. Role of persistent sodium current in bursting activity of mouse neocortical networks in vitro. *J. Neurophysiol.* 96:2564–2577. https://doi.org/10.1152/jn.00446.2006
Venkatesan, K., Y. Liu, and M. Goldfarb. 2014. Fast-onset long-term open-state block of sodium channels by A-type FHFs mediates classical spike accommodation in hippocampal pyramidal neurons. *J. Neurosci.* 34:16126–16139. https://doi.org/10.1523/JNEUROSCI.1271-14.2014
Vervaeke, K., H. Hu, L.J. Graham, and J.F. Storm. 2006. Contrasting effects of the persistent Na+ current on neuronal excitability and spike timing. *Neuron.* 49:257–270. https://doi.org/10.1016/j.neuron.2005.12.022
Wenninger, J.M., L.G. Pan, L. Klum, T. Leekley, J. Bastastic, M.R. Hodges, T.R. Feroah, S. Davis, and H.V. Forster. 2004. Large lesions in the pre-Bötzinger complex area eliminate eupneic respiratory rhythm in awake goats. *J. Appl. Physiol.* 97:1629–1636. https://doi.org/10.1152/japplphysiol.00953.2003
Wu, N., A. Enomoto, S. Tanaka, C.-F. Hsiao, D.Q. Nykamp, E. Izhikevich, and S.H. Chandler. 2005. Persistent sodium currents in mesencephalic v neurons participate in burst generation and control of membrane excitability. *J. Neurophysiol.* 93:2710–2722. https://doi.org/10.1152/jn.00636.2004
Yamada-Hanff, J., and B.P. Bean. 2013. Persistent sodium current drives conditional pacemaking in CA1 pyramidal neurons under muscarinic stimulation. *J. Neurosci.* 33:15011–15021. https://doi.org/10.1523/JNEUROSCI.0577-13.2013
Yue, C., S. Remy, H. Su, H. Beck, and Y. Yaari. 2005. Proximal persistent Na+ channels drive spike afterdepolarizations and associated bursting in adult CA1 pyramidal cells. *J. Neurosci.* 25:9704–9720. https://doi.org/10.1523/JNEUROSCI.1621-05.2005
Zavala-Tecuapetla, C., M.A. Aguileta, J.J. Lopez-Guerrero, M.C. González-Marín, and F. Peña. 2008. Calcium-activated potassium currents differentially modulate respiratory rhythm generation. *Eur. J. Neurosci.* 27:2871–2884. https://doi.org/10.1111/j.1460-9568.2008.06214.x
Zhong, G., M.A. Masino, and R.M. Harris-Warrick. 2007. Persistent sodium currents participate in fictive locomotion generation in neonatal mouse spinal cord. *J. Neurosci.* 27:4507–4518. https://doi.org/10.1523/JNEUROSCI.0124-07.2007
Ziskind-Conhaim, L., L. Wu, and E.P. Wiesner. 2008. Persistent sodium current contributes to induced voltage oscillations in locomotor-related hb9 interneurons in the mouse spinal cord. *J. Neurophysiol.* 100:2254–2264. https://doi.org/10.1152/jn.90437.2008